

Development of an *ab initio* method for exciton condensation and its application to TiSe₂Hsiao-Yi Chen ¹, Takuya Nomoto ², and Ryotaro Arita ^{1,2}¹RIKEN Center for Emergent Matter Science (CEMS), Wako 351-0198, Japan²Research Center for Advanced Science and Technology, University of Tokyo, Komaba Meguro-ku, Tokyo 153-8904, Japan

(Received 23 August 2022; accepted 5 November 2023; published 27 November 2023)

Exciton condensation is a phenomenon that indicates the spontaneous formation of electron-hole pairs, which can lead to a phase transition from a semimetal to an excitonic insulator by opening a gap at the Fermi surface. Although the idea of an excitonic insulator has been proposed for several decades, current theoretical approaches can only provide qualitative descriptions, and a quantitative predictive tool is still lacking. To shed light on this issue, we developed an *ab initio* method based on finite-temperature density functional theory and many-body perturbation theory to calculate the critical behavior of exciton condensation. Utilizing our methodology on monolayer TiSe₂, we identify a phase transition involving lattice distortion and nontrivial electron-hole correlation at a temperature exceeding the critical temperature of phonon softening. By breaking down the components within the gap equation, we demonstrate that exciton condensation, mediated by electron-phonon interaction, is the underlying cause of the charge-density-wave state observed in this compound. Overall, the methodology introduced in this work is general and sets the stage for searching for potential excitonic insulators in natural material systems.

DOI: [10.1103/PhysRevResearch.5.043183](https://doi.org/10.1103/PhysRevResearch.5.043183)

I. INTRODUCTION

The formation of fermion pairs can break the limit of the Pauli exclusion principle, accepting particles to occupy the same quantum state. At low temperatures, the coherent occupation can reshape the electronic structure and lead to a phase transition. The most well-known example in metallic materials is the Bardeen-Cooper-Schrieffer (BCS) theory of superconductivity [1], where the paired electrons, known as Cooper pairs, create a gap that enables frictionless transport and triggers superconductivity. In contrast, in a semimetal or a semiconductor with a narrow band gap, an electron in the conduction band may pair with a hole in the valence band to produce an exciton. The condensation of excitons in the ground state leads to the formation of the excitonic insulator (EI) [2–5].

The phenomenon of EI has been extensively investigated under various pairing conditions, spanning from weak coupling BCS-like scenarios [4] to strongly coupled Bose-Einstein condensation [6–8], with pairing forces beyond the Coulomb attraction [9–11]. Researchers have proposed methods as an analogy of superconductivity theory by replacing the superconducting order parameter $\chi = \langle \psi_e \psi_e \rangle$ with the thermal expectation value of exciton operator $\chi^{\text{ex}} = \langle \psi_e \psi_h \rangle$. However, after several decades since its inception, the experimental search for excitonic insulators still lags behind. At present, exciton condensation is primarily observed in

artificial quantum well and bilayer structures or induced by pressure and photoexcitation [12–21]. Conversely, natural cases are only found in the pristine crystals of some transition metal compounds [22–27].

Among them, 1T-TiSe₂ in the bulk form is known to undergo structural phase transition from a disorder state to a commensurate $2 \times 2 \times 2$ charge-density-wave (CDW) state when the temperature is decreased below the critical value $T_c \sim 190$ K [27–32]. The phase transition is characterized by the mixing of the Se $4p$ and Ti $3d$ bands observed by ARPES [31,32] and the occurrence of phonon softening, as revealed by x-ray diffuse scattering [33]. However, these observations are insufficient and sometimes controversial for understanding the fundamental mechanism behind the CDW order, for which theorists argued between the band Jahn-Teller effect [34–36] and exciton condensation [23,27,32,37–43]. This puzzle lasted until the recent experiment, where a soft-plasmon mode that appears exclusively in the EI phase was observed using the momentum-resolved electron energy-loss (EEL) spectroscopy [27]. In recent years, with the development of the two-dimensional synthesis technique, 1T-TiSe₂ in its monolayer form is raising a new trend to study the EI/CDW properties [44–50] and its relation to superconductivity [51].

In contrast to the versatile model development and bountiful experimental evidence, numerical methods to compute EI from first principles are remarkably lacking. Current approaches using density functional theory (DFT) based on the local exchange-correlation (XC) function such as the local density approximation (LDA), generalized gradient approximation (GGA), or hybrid functional [52–55] are capable of describing the ground-state structure of ordered and disordered phases [56–59] but not the evolution as a function

Published by the American Physical Society under the terms of the Creative Commons Attribution 4.0 International license. Further distribution of this work must maintain attribution to the author(s) and the published article's title, journal citation, and DOI.

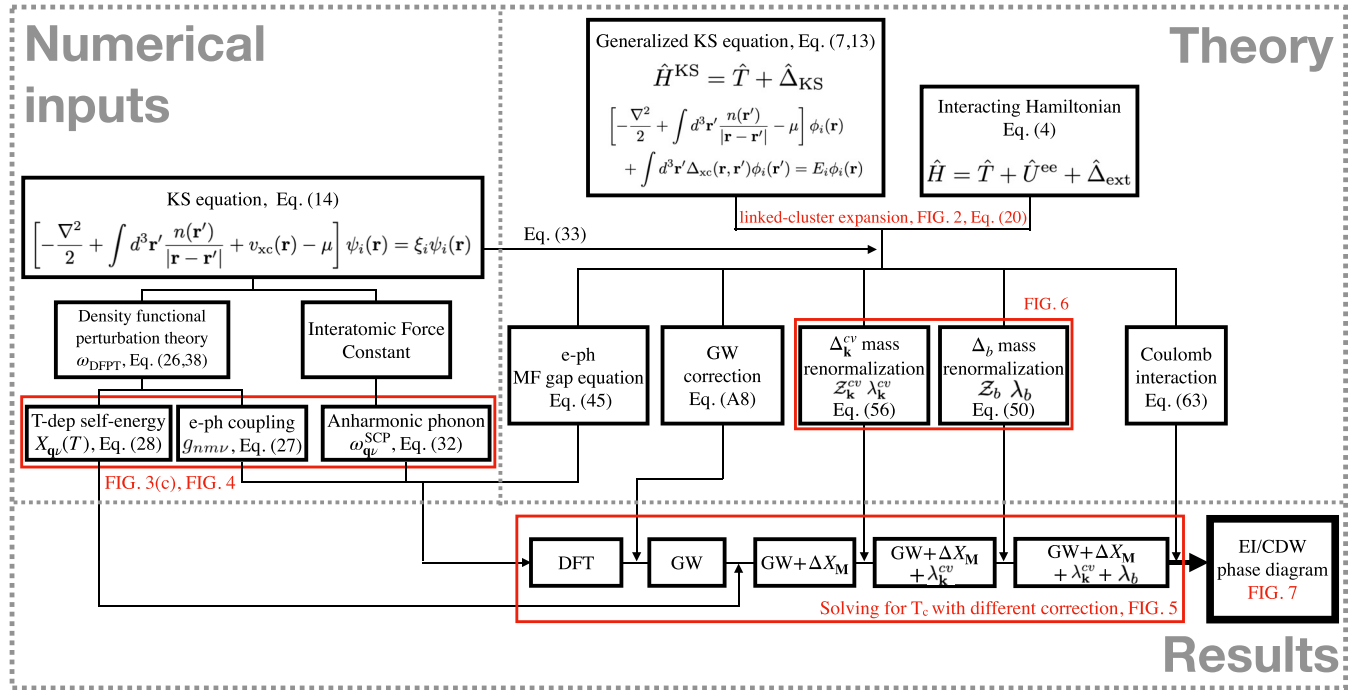


FIG. 1. The structure and workflow of this paper. Upper-right panel: We extend Kohn-Sham’s formalism of DFT by incorporating the nonlocal (NL) charge density and potential. Using the linked-cluster expansion, we demonstrate that the NL potential contributes to an energy modification equivalent to the GW correction and derive a gap equation with mass renormalization that can describe the exciton condensation phenomenon accompanied by lattice distortion, as discussed in Secs. II and III. Upper-left panel: We implement the gap equation with numerical data from standard DFT and DFPT, including the KS energy, anharmonic phonon frequency, e -ph coupling, and screened Coulomb interaction, computed by existing first-principles packages. Bottom panel: Combining the theory and numerical inputs, we investigate the exciton condensation in monolayer TiSe_2 . We perform computations by considering different corrections within the formalism step by step and present the EI/CDW phase diagram as the final result. The detailed discussion is presented in Sec. IV C.

of temperature. Some examples extend DFT with electron and hole in equal footing to construct the XC functional for studying excitonic superfluid [60,61]. Another study uses the GW and Bethe-Salpeter equation (BSE) method to construct the Bogoliubov–de-Gennes equation and calculate the EI gap function at finite temperature [62]. However, these approaches only consider the Coulomb attraction, overlooking the interplay between electron density and crystal structure.

In this paper, we present a systematic approach to studying exciton condensation by promoting the EI order parameter to a generalized nonlocal (NL) density and constructing a DFT scheme, as inspired by superconductivity density functional theory (SCDFT) [63,64]. To investigate the possible atomic displacement in the ordered phase, we adopt the Born-Oppenheimer approximation with additional linear potential and take into account the anharmonicity. Treating the electron and phonon on equal footing, we use the many-body perturbation method to compute the self-consistent NL XC functional and derive the gap equation to investigate the critical behavior. We perform numerical implementation for monolayer TiSe_2 based on the formalism and discuss the critical component for calculating the transition temperature. Our calculations demonstrate that the critical temperature for exciton condensation induced by electron-phonon coupling is higher than the temperature at which phonon softening occurs. This outcome supports the conclusion that the lattice distortion and CDW order in monolayer TiSe_2 are primarily driven by exciton condensation, rather than the instability of anharmonic phonons.

Our work presents a broadly applicable approach to access the microscopic mechanism of exciton condensation and sheds light on the numerical method for revealing the EI phase in materials.

The paper is organized as follows. In Sec. II we develop our *ab initio* method to describe exciton condensation and provide a brief review on phonon self-energy. In Sec. III we derive the gap equation for the EI/CDW state caused by electron-phonon (e -ph) coupling and the Coulomb interaction. In Sec. IV we applied the formalism and carry out numerical calculation to study the EI/CDW phase in monolayer TiSe_2 . We summarize the results and discuss future research in Sec. V. In the Appendices, we left derivations and numerical details in the appendices. Overall, the structure of this paper and the workflow of the framework is summarized in Fig. 1.

II. THEORY

In this section, we will describe the formulation used in this work. We introduce a DFT formalism with a generalized NL density that characterizes spontaneous fermion pairing. The XC functional and ground-state structure can be obtained self-consistently at finite temperature using the thermodynamical method. We then extend the discussion by including the phonon degree of freedom. In order to study CDW, we introduce a linear distortion potential in the phonon Hamiltonian. Before proceeding, we provide a brief summary of phonon self-energy and the self-consistent phonon (SCP) theory [65],

which is dominated by the anharmonic phonon-phonon interaction. Ultimately, the theories we develop and use here will be applied to investigate exciton condensation from first principles in the following section.

A. DFT with generalized nonlocal density

The *ab initio* approach adopted in this work is based on the multicomponent DFT [66]. By generalizing the electronic density, this approach has opened the gate to computing molecule bonding length, magnetization, and superconductivity from first principles [66–68]. Starting from the many-electron interacting Hamiltonian

$$\hat{H} = \hat{T} + \hat{U}^{ee} + \hat{V}_{\text{ext}}, \quad (1)$$

where the \hat{T} is the electronic kinetic energy, \hat{U}^{ee} is the Coulomb interaction among electron gas, and \hat{V}_{ext} is the external field including the potential from the nuclei. The Kohn-Sham (KS) method [69] replaces the many-body interaction by a local potential and writes an effective single-particle Hamiltonian:

$$\hat{H}^{\text{KS}} = \hat{T} + \hat{V}_{\text{KS}} = \hat{T}[n] + \hat{V}_H[n] + \hat{V}_{\text{XC}}[n] + \hat{V}_{\text{ext}}[n] \quad (2)$$

where \hat{V}_H is the Hartree term, \hat{V}_{XC} is the XC potential, and \hat{V}_{ext} comes from the external field. The Eq. (2) can reproduce the same ground-state energy as Eq. (1) with the same local electronic density according to the Hohenberg-Kohn theorem [70]. Thus, if we have the true XC potential, then we can obtain the exact solution for the target system, but \hat{V}_{XC} can only be acquired approximately.

In correlated systems, like superconductor [64,68], the local potential is insufficient to represent the many-body interaction, and NL potential and density must be adopted to characterize the electronic order. Here we start from a DFT with the NL charge densities $\chi(\mathbf{r}, \mathbf{r}')$ in the form:

$$\chi(\mathbf{r}, \mathbf{r}') = \sum_{\sigma} \langle \Psi_{\sigma}^{\dagger}(\mathbf{r}) \Psi_{\sigma}(\mathbf{r}') \rangle, \quad (3)$$

where Ψ_{σ} is the electron operator, σ denotes the spin index, and $\langle A \rangle = \text{Tr}[e^{-\beta H} A]$ defines the thermal expectation value [71]. Note that when the two position are identified, Eq. (3) reduces to the local density, $\chi(\mathbf{r}, \mathbf{r}) = n(\mathbf{r})$. Therefore, following the KS construction of DFT, we can include possible external potential acting on the NL charge density by considering the Hamiltonian:

$$\hat{H} = \hat{T} + \hat{U}^{ee} + \hat{\Delta}_{\text{ext}}, \quad (4)$$

where

$$\hat{\Delta}_{\text{ext}} = \sum_{\sigma} \int d^3\mathbf{r} \Psi_{\sigma}^{\dagger}(\mathbf{r}) \Delta_{\text{ext}}(\mathbf{r}, \mathbf{r}') \Psi_{\sigma}(\mathbf{r}'). \quad (5)$$

At finite temperature, this Hamiltonian reproduces the thermodynamic potential as a functional NL charge density:

$$\begin{aligned} \Omega[\chi] = & F[\chi] - \mu \int d^3\mathbf{r} d^3\mathbf{r}' \delta(\mathbf{r} - \mathbf{r}') \chi(\mathbf{r}, \mathbf{r}') \\ & + \int d^3\mathbf{r} d^3\mathbf{r}' [\chi(\mathbf{r}, \mathbf{r}') \Delta_{\text{ext}}(\mathbf{r}, \mathbf{r}') + \text{H.c.}], \end{aligned} \quad (6)$$

where the free energy $F[\chi]$ is universal and independent from external potentials and μ is the chemical potential acting on the local part of $\chi(\mathbf{r}, \mathbf{r}')$ [72].

Compared to the interacting Hamiltonian, Eq. (4), we can write the corresponding KS Hamiltonian of noninteracting orbitals [69]:

$$\hat{H}^{\text{KS}} = \hat{T} + \hat{\Delta}_{\text{KS}}, \quad (7)$$

and the thermodynamic potential becomes

$$\begin{aligned} \Omega^{\text{KS}}[\chi] = & F^{\text{KS}}[\chi] + \int d^3\mathbf{r} d^3\mathbf{r}' \Delta_{\text{KS}}(\mathbf{r}, \mathbf{r}') \chi(\mathbf{r}, \mathbf{r}') \\ & - \mu \int d^3\mathbf{r} d^3\mathbf{r}' \delta(\mathbf{r} - \mathbf{r}') \chi(\mathbf{r}, \mathbf{r}'), \end{aligned} \quad (8)$$

where $F^{\text{KS}}[\chi]$ is the free energy of noninteracting KS system. To make the KS Hamiltonian, Eq. (7), reproduce the same thermal ground state as the interacting system, both thermodynamic potentials must be minimized by the same ground-state densities:

$$\begin{aligned} \frac{\partial \Omega}{\partial \chi(\mathbf{r}, \mathbf{r}')} = & \frac{\partial F}{\partial \chi(\mathbf{r}, \mathbf{r}')} + \Delta_{\text{ext}}(\mathbf{r}, \mathbf{r}') - \mu \delta(\mathbf{r} - \mathbf{r}') = 0 \\ \frac{\partial \Omega^{\text{KS}}}{\partial \chi(\mathbf{r}, \mathbf{r}')} = & \frac{\partial F^{\text{KS}}}{\partial \chi(\mathbf{r}, \mathbf{r}')} + \Delta_{\text{KS}}(\mathbf{r}, \mathbf{r}') - \mu \delta(\mathbf{r} - \mathbf{r}') = 0. \end{aligned} \quad (9)$$

By defining the XC-free energy to satisfy the relation:

$$F[\chi] = F^{\text{KS}}[\chi] + F_{\text{XC}}[\chi] + \frac{1}{2} \int d^3\mathbf{r} d^3\mathbf{r}' \frac{n(\mathbf{r})n(\mathbf{r}')}{|\mathbf{r} - \mathbf{r}'|} \quad (10)$$

and the exchange-correlation potential:

$$\Delta_{\text{xc}}[\chi](\mathbf{r}, \mathbf{r}') \equiv \frac{\partial F_{\text{XC}}}{\partial \chi(\mathbf{r}, \mathbf{r}')} \quad (11)$$

we identify the nonlocal potential of the two systems:

$$\begin{aligned} \Delta_{\text{KS}}(\mathbf{r}, \mathbf{r}') = & \Delta_{\text{ext}}(\mathbf{r}, \mathbf{r}') + \Delta_{\text{xc}}(\mathbf{r}, \mathbf{r}') \\ & + \delta(\mathbf{r}, \mathbf{r}') \int d^3\mathbf{r}'' \frac{n(\mathbf{r}'')}{|\mathbf{r} - \mathbf{r}''|}. \end{aligned} \quad (12)$$

Therefore, by taking $\Delta_{\text{ext}} = 0$, we can write the generalized KS equation [73]:

$$\begin{aligned} \left[-\frac{\nabla^2}{2} + \int d^3\mathbf{r}' \frac{n(\mathbf{r}')}{|\mathbf{r} - \mathbf{r}'|} - \mu \right] \phi_i(\mathbf{r}) \\ + \int d^3\mathbf{r}' \Delta_{\text{xc}}(\mathbf{r}, \mathbf{r}') \phi_i(\mathbf{r}') = E_i \phi_i(\mathbf{r}). \end{aligned} \quad (13)$$

To compare with the standard KS equation [74]:

$$\left[-\frac{\nabla^2}{2} + \int d^3\mathbf{r}' \frac{n(\mathbf{r}')}{|\mathbf{r} - \mathbf{r}'|} + v_{\text{xc}}(\mathbf{r}) - \mu \right] \psi_i(\mathbf{r}) = \xi_i \psi_i(\mathbf{r}), \quad (14)$$

where the potential is local

$$v_{\text{xc}}[n](\mathbf{r}) \equiv \left. \frac{\partial F_{\text{XC}}}{\partial \chi(\mathbf{r}, \mathbf{r}')} \right|_{\chi(\mathbf{r} \neq \mathbf{r}')=0} \quad (15)$$

and generally evaluated with LDA or GGA method, we isolate $v_{xc}(\mathbf{r})$ from the nonlocal part in Eq. (13) and obtain

$$\begin{aligned} & \left[-\frac{\nabla^2}{2} + \int d^3\mathbf{r}' \frac{n(\mathbf{r}')}{|\mathbf{r}-\mathbf{r}'|} + v_{xc}(\mathbf{r}) - \mu \right] \phi_i(\mathbf{r}) \\ & + \int d^3\mathbf{r}' [\Delta_{xc}(\mathbf{r}, \mathbf{r}') - \delta(\mathbf{r}-\mathbf{r}')v_{xc}(\mathbf{r})] \phi_i(\mathbf{r}') = E_i \phi_i(\mathbf{r}). \end{aligned} \quad (16)$$

This is the major result of this section. The first line in Eq. (16) is identical to the standard KS-equation, Eq. (14), while the second line represents the contribution from fully nonlocal part, $\mathbf{r} \neq \mathbf{r}'$, and causes mixing among standard KS orbitals, ψ_i 's. Using the eigenfunctions of Eq. (14) as a basis set, we can project Eq. (16) on ψ_i and obtain:

$$\begin{aligned} & \xi_j t_j^i + \sum_k t_k^i \int d^3\mathbf{r} d^3\mathbf{r}' \psi_j^*(\mathbf{r}) \\ & \times [\Delta_{xc}(\mathbf{r}, \mathbf{r}') - \delta(\mathbf{r}-\mathbf{r}')v_{xc}(\mathbf{r})] \psi_k(\mathbf{r}') = E_i t_j^i, \end{aligned} \quad (17)$$

where we defined the mixing coefficient t_j^i :

$$t_j^i = \int d^3\mathbf{r} \psi_j^*(\mathbf{r}) \phi_i(\mathbf{r}), \quad (18a)$$

$$\phi_i(\mathbf{r}) = \sum_j t_j^i \psi_j(\mathbf{r}), \quad (18b)$$

such that the solving Eq. (16) reduces to a linear algebra problem, with eigenvector t_j^i and eigenvalue E_i . This derivation is general for all NL-densities beyond the definition in Eq. (3). For example, by choosing $\chi(\mathbf{r}, \mathbf{r}') = \langle \Psi_\uparrow(\mathbf{r}) \Psi_\downarrow(\mathbf{r}') \rangle$, i.e., the Cooper pairing, we can obtain the DFT for superconductivity [64,68].

Based on Eq. (16), once the form of the XC potential is known, we can determine the ground-state structure. In this study, we adopted a similar approach to SCDFPT [63,64] and employed the KS perturbation theory [75] to determine the Δ_{xc} . By identifying the KS Hamiltonian, Eq. (7), as the unperturbed part from the interacting Hamiltonian, Eq. (4), we obtain a perturbation theory:

$$\hat{H}_0 = \hat{H}^{\text{KS}}; \quad \hat{H}_I = \hat{U}^{\text{ee}} - \hat{\Delta}_{\text{KS}}. \quad (19)$$

Using Eq. (19) the difference between the interacting and KS thermodynamic potential can be expanded using the linked-cluster theorem [76–78] as:

$$\Omega = \Omega^{\text{KS}} - \frac{1}{\beta} \sum_{l=1}^{\infty} U_l, \quad (20)$$

where U_l are different connected Feynman diagrams generated by \hat{H}_I [79]. According to Eq. (9), both thermal potentials are minimized by the ground-state density such that the derivative of Eq. (20) must vanish:

$$\frac{\partial}{\partial \chi} (\Omega - \Omega^{\text{KS}}) = 0 = \sum_{l=1}^{\infty} \frac{\partial U_l}{\partial \chi}. \quad (21)$$

This is one of the major condition in this work that will be applied to derive the gap equation in Sec. III. In Appendix A, we demonstrate that this method can also be utilized to obtain the GW correction, which is typically derived from the Green's function approach [80].

B. DFT with generalized density from phonon degree of freedom

To discuss the structural transition, we must consider a theory that involves the atomic degree of freedom. In this work, we restrict the discussion to the Born-Oppenheimer approximation, which employs the phonon vibration to represent atomic motion. The standard approach expands the interatomic potential from the equilibrium structure in the Taylor series, where the lowest quadratic term defines the noninteracting phonon normal mode while higher-order terms take account of the anharmonic phonon-phonon (ph-ph) interactions [81]. Consequently, the spontaneous lattice distortion can be characterized by the thermal average of the phonon operator, which is proportional to the static atomic displacement.

To accommodate the lattice deformation, we extend the KS Hamiltonian by introducing a phonon Hamiltonian:

$$\hat{H}_{\text{ph}} = \hat{H}_{0,\text{ph}} + \hat{U}_{\text{anh.}}^{\text{ph}} + \hat{U}^{e\text{-ph}} + \hat{\Delta}_b \quad (22)$$

where the free phonon Hamiltonian $\hat{H}_{0,\text{ph}}$, ph-ph anharmonic interaction $\hat{U}_{\text{anh.}}^{\text{ph}}$, and e -ph interaction $\hat{U}^{e\text{-ph}}$ are defined as standard forms as in literature [65,82]. The last term denotes a linear deformation potential of the form:

$$\hat{\Delta}_b = \sum_{\mathbf{q}\nu} (\Delta_{b,\mathbf{q}\nu}^* \hat{b}_{\mathbf{q}\nu} + \Delta_{b,\mathbf{q}\nu} \hat{b}_{\mathbf{q}\nu}^\dagger), \quad (23)$$

which can push atoms away from their equilibrium position without phonon softening when the phonon frequency remains real, $\omega^2 > 0$. Therefore, the phonon operator acquires a finite thermal average:

$$\langle \hat{b}_{\mathbf{q}\nu} \rangle = \chi_{b,\mathbf{q}\nu} \quad (24)$$

such that if we treat $\chi_{b,\mathbf{q}\nu}$ on the same footing as the densities in Eq. (3), the Δ_b 's can be determined by the perturbation expansion method introduced in the previous section where the Hamiltonian now includes the phonon degree of freedom:

$$\hat{H} = \hat{H}_0 + \hat{H}_I, \quad (25a)$$

$$\hat{H}_0 = \hat{T} + \hat{\Delta}_{\text{KS}} + \hat{H}_{0,\text{ph}} + \hat{\Delta}_b, \quad (25b)$$

$$\hat{H}_I = \hat{U}^{\text{ee}} - \hat{\Delta}_{\text{KS}} + \hat{U}_{\text{anh.}}^{\text{ph}} + \hat{U}^{e\text{-ph}} - \hat{\Delta}_b. \quad (25c)$$

This is the general formalism used to describe lattice deformation at finite temperature. The distorted pattern follows the phonon normal vector, which is denoted by the mode index ν . The displacement amplitude is proportional to the absolute value of $\chi_{b,\mathbf{q}\nu}$, and the momentum \mathbf{q} determines the periodicity of the new crystal structure. In Sec. III, we will apply Eqs. (25a)–(25c) to derive the gap equation for the exciton condensation phenomenon.

C. Phonon self-energy from first principles

This section provides a discussion of the phonon properties obtained through first-principles approaches. The *ab initio* phonon vibration can be calculated by diagonalizing the dynamical matrix, which describes the total energy change when atoms move away from their equilibrium positions. The dynamical matrix can be computed practically using density functional perturbation theory (DFPT) [81] or the frozen phonon method [83]. Phonon frequencies obtained by these

methods contain the “bare” part as well as the renormalization effect [84–86]:

$$\omega_{\mathbf{q}\nu}^2 = \omega_{\mathbf{q}\nu}^{\text{bare}^2} + 2\omega_{\mathbf{q}\nu}^{\text{bare}} \Pi_{\mathbf{q}\nu}^{\text{bare}}(T), \quad (26a)$$

$$\Pi_{\mathbf{q}\nu}^{\text{bare}}(T) = \frac{2}{\mathcal{N}_k} \sum_{\mathbf{k}mn} |g_{m\nu\nu}^{\text{bare}}(\mathbf{k}, \mathbf{q})|^2 \frac{f_{\mathbf{k}+\mathbf{q},m} - f_{\mathbf{k},n}}{\xi_{\mathbf{k}+\mathbf{q}}^m - \xi_{\mathbf{k}}^n}, \quad (26b)$$

where $g_{m\nu\nu}^{\text{bare}}(\mathbf{k}, \mathbf{q})$ is the bare e -ph matrix element:

$$g_{m\nu\nu}^{\text{bare}}(\mathbf{k}, \mathbf{q}) = \left(\frac{\hbar}{2\omega_{\mathbf{q}\nu}^{\text{bare}}} \right)^{1/2} \langle \psi_{m\mathbf{k}+\mathbf{q}} | \partial_{\mathbf{q}\nu} V | \psi_{n\mathbf{k}} \rangle. \quad (27)$$

In Eq. (26b), $\Pi_{\mathbf{q}\nu}^{\text{bare}}$ is the self-energy due to the Coulomb screening, where the superscript “bare” denotes that we used the bare coupling constant from Eq. (27), and the factor of 2 appears for the spin degeneracy [87]. \mathcal{N}_k is the number of k points, $\xi_{\mathbf{k}}^n$ is the electron energy of the n th band with momentum \mathbf{k} measured from the chemical potential, and $f_{\mathbf{k},n} = 1/(e^{\beta\xi_{\mathbf{k}}^n} + 1)$ is the Fermi-Dirac distribution function. Here we note that although the self-energy depends on the phonon frequency via the coupling constant, the renormalization only depends on the deformation potential $\partial_{\mathbf{q}\nu} V$ and the electronic occupations $f_{\mathbf{k},n}$. Therefore, for later use, we define a frequency-independent factor,

$$X_{\mathbf{q}\nu}(T) = \frac{\hbar}{\mathcal{N}_k} \sum_{\mathbf{k}mn} |\langle \psi_{m\mathbf{k}+\mathbf{q}} | \partial_{\mathbf{q}\nu} V | \psi_{n\mathbf{k}} \rangle|^2 \frac{f_{\mathbf{k}+\mathbf{q},m} - f_{\mathbf{k},n}}{\xi_{\mathbf{k}+\mathbf{q}}^m - \xi_{\mathbf{k}}^n}, \quad (28)$$

such that the phonon frequency difference between two temperatures due to the screening effect can be written as

$$\omega_{\mathbf{q}\nu}^2(T_1) - \omega_{\mathbf{q}\nu}^2(T_2) = 2X_{\mathbf{q}\nu}(T) \Big|_{T_2}^{T_1}, \quad (29)$$

where we neglect the temperature dependence in the deformation potential.

In general, experimental observables are fully renormalized quantities, so researchers typically focus on explaining the direct results ω as experimental measurements, while the isolation between the bare frequency ω^{bare} and self-energy is rarely studied [88]. However, when a single phonon momentum \mathbf{q} connects the electron pocket and hole pocket in some metallic systems, $\Pi_{\mathbf{q}\nu}$ tends to diverge. This divergence forces the corresponding renormalized phonon to become soft with imaginary frequency, as the self-energy is always negative. This so-called Fermi-surface nesting effect destabilizes the crystal structure, resulting in lattice distortion and causing a transition into a CDW phase.

The phonons obtained from the above method are restricted to the harmonic approximation, which expands the energy variation up to the second order of atomic displacement. While the harmonic phonon approach has achieved considerable success in studying transport properties, carrier relaxation, and polaronic systems [89–91], it is inadequate in describing many critical properties associated with lattice anharmonicity, such as thermal expansion, lattice transition, temperature-dependent phonon frequency, and prediction of critical temperature for superconductivity [92–97].

In this work, we adopt the SCP theory [65,98] to compute the anharmonic phonon frequency. The SCP theory expands

the energy to quartic order of the atomic displacement [99]:

$$U_n = \frac{1}{n!} \left(\frac{\hbar}{2} \right)^{\frac{n}{2}} \sum_{\{q_n\}} \delta(\Sigma \mathbf{q}_n, \mathbf{G}) \frac{\Phi(q_1, \dots, q_n)}{\sqrt{\omega_{q_1} \dots \omega_{q_n}}} \hat{A}_{q_1} \dots \hat{A}_{q_n} \quad (30)$$

where U_n is the energy manifold when moving n atoms away from their equilibrium position, $q = (\mathbf{q}, \nu)$ is the collective index, $\delta(\Sigma \mathbf{q}_n, \mathbf{G})$ imposes the momentum conservation, $\Phi(q_1, \dots, q_n)$ is the interatomic force constant, and \hat{A}_q is the displacement operator. To the lowest order, the self-energy comes from the loop diagram of the four-points vertex:

$$\Sigma_{\mathbf{q},\nu\nu'} = -\frac{1}{2} \sum_{q_1} \frac{\hbar \Phi(\mathbf{q}\nu, -\mathbf{q}\nu', q_1, -q_1)}{4\sqrt{\omega_{\mathbf{q}\nu}^{\text{scp}} \omega_{-\mathbf{q}\nu'}^{\text{scp}} \omega_{q_1}^{\text{scp}}}} \times [1 + 2n_B(\omega_{q_1}^{\text{scp}})], \quad (31)$$

where n_B is the Bose-Einstein distribution function. This anharmonic self-energy contribution contains the mixing between different phonon normal modes ν, ν' such that it modifies both the phonon frequency and the vibration pattern. When the off-diagonal term can be neglected, the SCP equation can be simplified as:

$$\omega_{\mathbf{q}\nu}^{\text{scp}2} = \omega_{\mathbf{q}\nu}^2 + 2\omega_{\mathbf{q}\nu}^{\text{scp}} \Sigma_{\mathbf{q},\nu\nu}. \quad (32)$$

It has been shown that the SCP equation requires a real solution for all Ω 's such that the self-consistent solution breaks down when any phonon becomes soft.

III. EXCITON CONDENSATION

We apply the methods introduced in the previous section to study the EI/CDW phase. For a direct application to be discussed in the next section, we focus on the exciton formation between electron and hole with momentum $(\mathbf{k}_e, \mathbf{k}_h) = (\mathbf{k}, \mathbf{k} + \mathbf{M})$, where the transition momentum \mathbf{M} is chosen as $\mathbf{G}/2$, half of the reciprocal vector. The generalization to other transition momentum is straightforward and can be carried out following the same logic flow of this section. Focusing on the mixing among states of momentum \mathbf{k} and $\mathbf{k} + \mathbf{M}$, we rewrite the mixing function Eq. (18b) in the form of Bloch wave function:

$$\phi_{(\mathbf{k})}^n = \sum_{\nu} t_{\nu\mathbf{k}}^n \psi_{\nu\mathbf{k}} + \sum_c t_{c\mathbf{k}+\mathbf{M}}^n \psi_{c\mathbf{k}+\mathbf{M}} = \sum_i t_{i(\mathbf{k})}^n \psi_{i(\mathbf{k})}, \quad (33)$$

where we use ν to denote the band index for states with momentum \mathbf{k} , c to denote the band index for states with momentum $\mathbf{k} + \mathbf{M}$, and i for the mixed momentum \mathbf{k} and $\mathbf{k} + \mathbf{M}$ and make the notation as a convention throughout the paper. We note that, in this setting, we treat the occupied states and unoccupied states on an equal footing, and the c, ν indices are not restricted to valance bands or conduction bands. On the other hand, applying Eq. (33) to Eq. (3), the NL density becomes

$$\chi(\mathbf{r}, \mathbf{r}') = \sum_{ij(\mathbf{k})} \chi_{(\mathbf{k})}^{ij} \psi_{i(\mathbf{k})}^*(\mathbf{r}) \psi_{j(\mathbf{k})}(\mathbf{r}'), \quad (34a)$$

$$\chi_{(\mathbf{k})}^{ij} \equiv \sum_n f_{n(\mathbf{k})} t_{i(\mathbf{k})}^{n*} t_{j(\mathbf{k})}^n, \quad (34b)$$

where $\chi_{(\mathbf{k})}^{ij}$ evaluates the mixing between the i th and j th orbitals. The corresponding potential can be written as

$$\begin{aligned} \Delta_{(\mathbf{k})}^{ij} &= \int d^3\mathbf{r} d^3\mathbf{r}' \psi_{i(\mathbf{k})}^*(\mathbf{r}) \Delta(\mathbf{r}, \mathbf{r}') \psi_{j(\mathbf{k})}(\mathbf{r}') \\ &\quad - \int d^3\mathbf{r} \psi_{i(\mathbf{k})}^*(\mathbf{r}) v_{\text{xc}}(\mathbf{r}) \psi_{j(\mathbf{k})}(\mathbf{r}). \end{aligned} \quad (35)$$

For the mixing between states of momentum \mathbf{k} and $\mathbf{k} + \mathbf{M}$, the second line vanishes since

$$\begin{aligned} &\int d^3\mathbf{r} \psi_{v\mathbf{k}}^*(\mathbf{r}) v_{\text{xc}}(\mathbf{r}) \psi_{c\mathbf{k}+\mathbf{M}}(\mathbf{r}) \\ &= \sum_{n \in N} e^{-in\mathbf{M}\cdot\mathbf{a}} \int_{\text{BZ}} d^3\mathbf{r} u_{v\mathbf{k}}^*(\mathbf{r}) v_{\text{xc}}(\mathbf{r}) u_{c\mathbf{k}+\mathbf{M}}(\mathbf{r}) = 0, \end{aligned} \quad (36)$$

where we use the periodic property of $v_{\text{xc}}(\mathbf{r}) = v_{\text{xc}}(\mathbf{r} + \mathbf{a})$ and \mathbf{a} is the lattice constant in normal phase. On the other hand, for the mixing between states of the same momentum, we follow the GWA which accounts only for the diagonal part as presented in Appendix A. In the following, we will simplify the subscription $\chi_{(\mathbf{k})}^{ij}$, $\Delta_{(\mathbf{k})}^{ij} \rightarrow \chi_{\mathbf{k}}^{ij}$, $\Delta_{\mathbf{k}}^{ij}$ for density and potential without raising any confusion.

For the phonon sector we attribute the phase transition to a single phonon mode ν_0 such that the phonon distortion potential Eq. (23) can be reduced to the subspace:

$$\hat{\Delta}_b = \Delta_b^* \hat{b}_{\mathbf{M}\nu_0} + \Delta_b \hat{b}_{\mathbf{M}\nu_0}^\dagger. \quad (37)$$

In practical implementation, we do not directly use Eq. (25a)–(25c). Since the DFPT calculation will always provide a screened phonon frequency as discussed in Sec. II C, we extract the screening part from \hat{H}_I and define the frequency adopted in the unperturbed Hamiltonian as

$$\omega_{\mathbf{q}\nu}^{\text{DFPT}} = \sqrt{\omega_{\mathbf{q}\nu}^{\text{bare}2} + 2X_{\mathbf{q}\nu}(T = 0 \text{ K})}, \quad (38)$$

which becomes imaginary when the phonon is soft. Besides, for the ph-ph anharmonic interactions, we take into account their contributions only in phonon frequency but neglect other scattering effects. Consequently, we can write an effective Hamiltonian for the perturbation theory:

$$\begin{aligned} \hat{H}_0 &= \sum_{\mathbf{k}} \xi_{\mathbf{k}}^n \hat{c}_{n\mathbf{k}}^\dagger \hat{c}_{n\mathbf{k}} + \sum_{\mathbf{q}, \nu} \omega_{\mathbf{q}\nu}^{\text{DFPT}} \hat{b}_{\mathbf{q}\nu}^\dagger \hat{b}_{\mathbf{q}\nu} + \tilde{\Delta}, \quad (39a) \\ \hat{H}_I &= \sum_{\mathbf{k}, \mathbf{q}, mn} g_{nm\nu}^{\text{DFPT}}(\mathbf{k}, \mathbf{q}) \hat{c}_{n\mathbf{k}+\mathbf{q}}^\dagger \hat{c}_{m\mathbf{k}} (\hat{b}_{-\mathbf{q}\nu}^\dagger + \hat{b}_{\mathbf{q}\nu}) + \text{c.c.} \\ &\quad + \sum_{\mathbf{q}, \nu\nu'} \tilde{\Pi}_{\mathbf{q}, \nu\nu'}(T) \hat{b}_{\mathbf{q}\nu}^\dagger \hat{b}_{\mathbf{q}\nu'} - \tilde{\Delta} + (\text{Coulomb}), \end{aligned} \quad (39b)$$

where (Coulomb) denotes $\hat{U}^{\text{ee}} - \hat{\Delta}_{\text{XC}}$ in Eq. (19), and we use the shorthands:

$$\tilde{\Delta} = \sum_{nm\mathbf{k}} \Delta_{\mathbf{k}}^{nm} \hat{c}_{n\mathbf{k}+\mathbf{M}}^\dagger \hat{c}_{m\mathbf{k}} + \Delta_b^* \hat{b}_{\mathbf{M}\nu_0} + \text{c.c.}, \quad (40a)$$

$$\tilde{\Pi}_{\mathbf{q}, \nu\nu'}(T) = \frac{\Omega_{\mathbf{q}\nu} \Sigma_{\mathbf{q}, \nu\nu'}(T) - \delta_{\nu\nu'} X_{\mathbf{q}\nu}(T = 0 \text{ K})}{\omega_{\mathbf{q}\nu}^{\text{DFPT}}}, \quad (40b)$$

where g^{DFPT} is the e -ph coupling constant we obtain from first-principles calculation:

$$g_{m\nu\nu}^{\text{DFPT}}(\mathbf{k}, \mathbf{q}) = \left(\frac{\hbar}{2\omega_{\mathbf{q}\nu}^{\text{DFPT}}} \right)^{1/2} \langle \psi_{m\mathbf{k}+\mathbf{q}} | \partial_{\mathbf{q}\nu} V | \psi_{n\mathbf{k}} \rangle, \quad (41)$$

which is different from Eq. (27) by a scaling prefactor depending on the phonon frequency. The self-energy $\Sigma(T)$ is required to be computed by Eq. (31), and the energy correction Eq. (40b) is chosen for the dressed phonon in this effective Hamiltonian matching the finite-temperature phonon such that the frequency satisfying the self-consistent equation:

$$\Omega_{\mathbf{q}\nu}^2 = \omega_{\mathbf{q}\nu}^{\text{DFPT}2} + 2X_{\mathbf{q}\nu}(T)|_{T=0} + 2\Omega_{\mathbf{q}\nu} \Sigma_{\mathbf{q}\nu}(T) \quad (42)$$

similarly to Eq. (32) in the diagonal approximation (see Appendix B).

Because the $\Omega_{\mathbf{q}\nu}(T)$ is the physical pole of the phonon Green's function and corresponds to the frequency measured in experiments, in the rest discussion, we will simply refer to "frequency" for this temperature-depending quantity without further specification and replace $\omega_{\mathbf{q}\nu}^{\text{DFPT}}$ by $\Omega_{\mathbf{q}\nu}(T)$ when computing the thermal average. Note that this substitution also changes the e -ph coupling constant due to the dependence on the phonon frequency via the relation:

$$g_{nm\nu}(\mathbf{k}, \mathbf{q}; T) = g_{nm\nu}^{\text{DFPT}}(\mathbf{k}, \mathbf{q}) \times \sqrt{\frac{\omega_{\mathbf{q}\nu}^{\text{DFPT}}}{\Omega_{\mathbf{q}\nu}(T)}}, \quad (43)$$

where we neglect the temperature effect on the deformation potential and normal mode eigenvector. This replacement of thermal quantities is already adopted in materials with anharmonic dynamics to study the carrier mobility [95].

In the following, we utilize Eqs. (39a) and (39b) to derive the formula for studying EI/CDW through computing diagrams presented in Fig. 2. We divide Fig. 2 into three categories and investigate their contribution separately. Figure 2(a) presents the lowest order diagrams consisting static terms of density and potentials, while Figs. 2(b)–2(e) are the self-energy part and bubble diagrams, which will provide the mass renormalization correction. Figures 2(f) and 2(g) represents the contribution due to the Coulomb interaction.

A. Gap equation

We first focus on Fig. 2(a) and derive the basic structure of the gap equation. The mathematical representation for the diagram is derived from the first line of Eq. (39b) and Eq. (40a):

$$\begin{aligned} U^{(a)} &= \sum_{c\nu\mathbf{k}} g_{c\nu\nu_0}(\mathbf{k}, \mathbf{M}) \langle \hat{c}_{c\mathbf{k}+\mathbf{M}}^\dagger \hat{c}_{\nu\mathbf{k}} \rangle \langle \hat{b}_{-\mathbf{M}\nu_0}^\dagger + \hat{b}_{\mathbf{M}\nu_0} \rangle \\ &\quad - \Delta_{\mathbf{k}}^{c\nu} \langle \hat{c}_{c\mathbf{k}+\mathbf{M}}^\dagger \hat{c}_{\nu\mathbf{k}} \rangle - \Delta_b^* \langle \hat{b}_{\mathbf{M}\nu_0} \rangle + \text{c.c.} \\ &= \sum_{c\nu\mathbf{k}} g_{c\nu\nu_0}(\mathbf{k}, \mathbf{M}) \chi_{\mathbf{k}}^{c\nu} (\chi_{b, \mathbf{M}\nu_0} + \chi_{b, \mathbf{M}\nu_0}^*) \\ &\quad - \Delta_{\mathbf{k}}^{c\nu} \chi_{\mathbf{k}}^{c\nu} - \Delta_b^* \chi_{b, \mathbf{M}\nu_0} + \text{c.c.}, \end{aligned} \quad (44)$$

where we have used the property $\hat{b}_{\mathbf{M}} = \hat{b}_{-\mathbf{M}}$ and Eq. (43) for the temperature depending on the e -ph coupling. We note that since all operators are equal time in terms of the Heisenberg picture, there is no propagator but only density. Applying

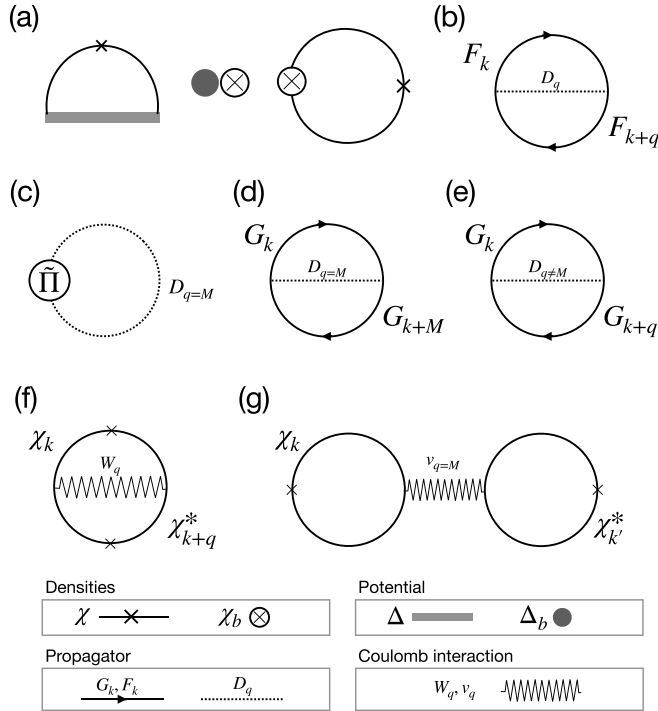


FIG. 2. Feynman diagrams based on the interacting Hamiltonian, Eq. (39b). (a) The lowest order diagrams in the linked-cluster expansion, containing products of MF density and potentials, from which we can derive the MF gap equation, Eq. (45). [(b)–(e)] Next-to-leading-order bubble diagrams resulting from the e -ph coupling, where $\hat{\Pi}$ is the self-energy defined in Eq. (40b). These diagram contribute to the mass renormalization terms, \mathcal{Z}_b and \mathcal{Z}_b^{cv} . The bottom column presents diagrams due to the Coulomb interaction. In (f), we consider the screened Coulomb interaction W_q while in (g) the bare Coulomb interaction is used. This choice of Coulomb interaction is inspired by Ref. [62]. The meaning of the symbols are summarized as follows: χ is the NL density [Eq. (34b)], χ_b is the phonon displacement [Eq. (24)], Δ is the NL potential [Eq. (35)], Δ_b is the phonon linear potential [Eq. (23)], G_k is the standard propagator without band change and momentum transfer [Eq. (52)], F_k is the anomalous propagator connecting state of momentum \mathbf{k} and $\mathbf{k} + \mathbf{M}$ [Eq. (46)], and D_q is the phonon propagator.

Eq. (44) to the minimum condition Eq. (21) in the lowest order, $U_{l=1} = U^{(a)}$, and keeping $\chi_{b,\mathbf{M}}(\chi_b)$ and $\chi_{b,\mathbf{M}}^*(\chi_b^*)$ as independent variables, we can obtain:

$$\Delta_b = \sum_{cv,\mathbf{k}} g_{cv\nu_0}(\mathbf{k}, \mathbf{M}) \chi_{\mathbf{k}}^{cv} + g_{cv\nu_0}^*(\mathbf{k}, \mathbf{M}) \chi_{\mathbf{k}}^{cv*}, \quad (45a)$$

$$\Delta_{\mathbf{k}}^{cv} = g_{cv\nu_0}(\mathbf{k}, \mathbf{M}) (\chi_{b,\mathbf{M}\nu_0} + \chi_{b,\mathbf{M}\nu_0}^*). \quad (45b)$$

These two equations are the same gap equations derived from the mean-field approach [9], and we will refer them as “MF gap equation” for the rest discussion. They can be solved consistently using the solution of Eq. (39a) and the definition in Eq. (24) and Eq. (34b). To present the detail, we carry out an example of an analytically solvable model in a one-dimensional system and discuss in Appendix C.

In the next order expansion of the linked cluster, Fig. 2(b) is induced by phonon-exchanging and consists of the anomalous

Green’s function [100]:

$$\hat{F}_{n(\mathbf{k})}(i\omega_n) = \sum_{cv} \frac{t_{v\mathbf{k}}^{n*} t_{c\mathbf{k}+\mathbf{M}}^{n*} |v\mathbf{k}\rangle \langle c\mathbf{k} + \mathbf{M}| + \text{H.c.}}{i\omega_n - E_{n(\mathbf{k})}}. \quad (46)$$

This diagram contains internal phonon propagator, $D_{\mathbf{q}}$, of general momentum \mathbf{q} and contributes to the gap equation by a term proportional to

$$\propto \frac{1}{\mathcal{N}_q} \sum_{c'v',\mathbf{q},\nu} g_{vv'\nu}(\mathbf{k} - \mathbf{q}, \mathbf{q}) g_{cc'\nu}^*(\mathbf{k} + \mathbf{M}, \mathbf{q}) \chi_{\mathbf{k}-\mathbf{q}}^{cv}. \quad (47)$$

However, in the studies with phonon softening, we can ignore Eq. (47) in computing the gap equation since the e -ph coupling for the soft-mode, $g_{cv\nu_0}(\mathbf{k}, \mathbf{M})$, is boosted by Eq. (43) and makes Eqs. (45a) and (45b) the dominant contributions.

B. Mass renormalization in Δ_b

The mass renormalization effect can be separated into two parts corresponding to the gap function Δ_b and $\Delta_{\mathbf{k}}$, respectively, and here we focus on the Δ_b . We isolate the $\mathbf{q} = \mathbf{M}$ part [Fig. 2(d)] from the bubble diagram [Fig. 2(e)] and combine it with the contribution from the effective self-energy term. To compute Fig. 2(d), we note that due to the $\hat{\Delta}$ potential term, the phonon operator $\hat{b}_{\mathbf{M}}^{(\dagger)}$ in the unperturbed Hamiltonian, Eq. (39a), acquires a nonzero thermal average such that its thermal Green’s function becomes (see Appendix D)

$$D_\nu(\mathbf{q}, i\omega_n) = \frac{-2\Omega_{\mathbf{q}\nu}}{\omega_n^2 + \Omega_{\mathbf{q}\nu}^2} - \delta_{\omega_n,0} \delta_{\mathbf{q},\mathbf{M}} \delta_{\nu,\nu_0} \frac{\beta(\Delta_b^* + \Delta_b)^2}{\Omega_{\mathbf{q}\nu}^2}. \quad (48)$$

The Green’s function now takes an additional static ($\omega_n = 0$) term for the ν_0 phonon with $\mathbf{q} = \mathbf{M}$ which is quadratically proportional to the potential Δ_b . Therefore, the Δ_b -relevant part of Figs. 2(c) and 2(d) becomes

$$U^{(c+d)} = \frac{(\Delta_b^* + \Delta_b)^2}{\Omega_{\mathbf{M}\nu_0}^2} \Pi_{\mathbf{M}\nu_0}(T) + \frac{|\Delta_b|^2}{\Omega_{\mathbf{M}\nu_0}^2} [\Sigma_{\mathbf{q},\nu\nu'}(T) - \Pi_{\mathbf{M}\nu_0}(T = 0 \text{ K})], \quad (49)$$

where $\Pi_{\mathbf{M}\nu_0}$ is defined as Eq. (26b) with the e -ph coupling replaced by Eq. (43). Using the relation Eq. (D2) and taking the derivative respective to χ_b^* , we can obtain

$$\frac{\partial U^{(c+d)}}{\partial \chi_b^*} = \frac{-2\Delta_b}{\Omega_{\mathbf{M}\nu_0}^2} [2\Omega_{\mathbf{M}\nu_0} \Sigma_{\mathbf{M}\nu_0}(T) + 2X_{\mathbf{M}\nu_0}(T)]_{T=0}^T \equiv -\mathcal{Z}_b \Delta_b. \quad (50)$$

The mass renormalization for the phonon displacement potential can thus be obtained by including Eq. (49) as the next-to-leading order correction in Eq. (21). Adding Eq. (50) to the right-hand side of Eq. (45a), the gap equation is modified by a overall ratio:

$$\Delta_b \equiv \lambda_b \left[\sum_{cv,\mathbf{k}} g_{cv\nu_0}(\mathbf{k}, \mathbf{M}) \chi_{\mathbf{k}}^{cv} + g_{cv\nu_0}^*(\mathbf{k}, \mathbf{M}) \chi_{\mathbf{k}}^{cv*} \right], \quad (51)$$

where $\lambda_b = 1/(1 + \mathcal{Z}_b)$. Since the factor \mathcal{Z}_b is always positive, the mass renormalization will reduce the displacement

potential and thus decrease the critical temperature for exciton condensation.

C. Mass renormalization in $\Delta_{\mathbf{k}}$

The mass renormalization on the NL potential $\Delta_{\mathbf{k}}$ can be obtained from Fig. 2(e) which is the bubble diagram involving only normal propagators, and here we include all the phonon momentum \mathbf{q} and normal modes ν . To compute Fig. 2(e), we first note that for the state of Eq. (33), the Green's function can be written as

$$\hat{G}_{n(\mathbf{k})}(i\omega_n) = \sum_{c\nu} \frac{|t_{\nu\mathbf{k}}^n|^2 |v\mathbf{k}\rangle\langle v\mathbf{k}| + |t_{c\mathbf{k}}^n|^2 |c\mathbf{k} + \mathbf{M}\rangle\langle c\mathbf{k} + \mathbf{M}|}{i\omega_n - E_{n(\mathbf{k})}}, \quad (52)$$

which already mixes states of momentum \mathbf{k} and $\mathbf{k} + \mathbf{M}$ following the Hamiltonian Eq. (39a). Therefore, Fig. 2(e) can be expressed as

$$U^{(e)} = \sum_{\mathbf{k}\mathbf{q}, nm, \nu} I(E_m(\mathbf{k}+\mathbf{q}), E_n(\mathbf{k}), \Omega_{\mathbf{q}\nu}) \times \left[\sum_{v_i v_j} |t_{v_i\mathbf{k}}^n|^2 |t_{v_j\mathbf{k}+\mathbf{q}}^m|^2 |g_{v_i v_j \nu}(\mathbf{k}, \mathbf{q})|^2 + \sum_{c_i c_j} |t_{c_i\mathbf{k}}^n|^2 |t_{c_j\mathbf{k}+\mathbf{q}}^m|^2 |g_{c_i c_j \nu}(\mathbf{k} + \mathbf{M}, \mathbf{q})|^2 \right], \quad (53)$$

where we define

$$I(E_1, E_2, \omega) = \sum_{\omega_n \omega_m} \frac{1}{i\omega_n - E_1} \frac{1}{i\omega_m - E_2} \frac{-2\omega}{(\omega_n - \omega_m)^2 + \omega^2}, \quad (54)$$

which is the common expression appearing in the bubble diagram including two fermions and one boson propagator. However, in a general system with bands of more than two, there is no analytical expression of coefficient $t_{\nu\mathbf{k}}^n$'s in terms of coupling potential $\Delta_{\mathbf{k}}$. As a result, we take the small $\Delta_{\mathbf{k}}$ approximation and use the perturbation theory to expand the coefficients. In the linear order, since the eigenvalue is the same as the diagonal entries, we can use the original band index to denote the new states such that

$$E_{n=v_i}(\mathbf{k}) = \xi_{\mathbf{k}}^{v_i}; t_{v_i\mathbf{k}}^{n=v_i} = \delta_{v_i, v_j}; t_{c_j\mathbf{k}}^{n=v_i} = \frac{\Delta_{\mathbf{k}}^{c_j v_i}}{\xi_{\mathbf{k}}^{v_i} - \xi_{\mathbf{k}+\mathbf{M}}^{c_j}} \\ E_{n=c_i}(\mathbf{k}) = \xi_{\mathbf{k}+\mathbf{M}}^{c_i}; t_{c_j\mathbf{k}}^{n=c_i} = \delta_{c_i, c_j}; t_{v_j\mathbf{k}}^{n=c_i} = \frac{\Delta_{\mathbf{k}}^{v_j c_i}}{\xi_{\mathbf{k}+\mathbf{M}}^{c_i} - \xi_{\mathbf{k}}^{v_j}}. \quad (55)$$

However, the linear order is insufficient to express the eigenvector terms in $U^{(e)}$ since the terms always appear as an absolute square, $|t_{c,v}^n|^2$. We compute the perturbation expansion to the second order for the explicit $\Delta_{\mathbf{k}}^{cv}$ dependence and take the derivative on Eq. (53). The algebraic detail is left to the Appendix E, and we quote the result here. The derivative

of the bubble diagram respective to NL densities can be written as

$$\frac{\partial U^{(e)}}{\partial \chi_{\mathbf{k}}^{cv}} = \frac{\Delta_{\mathbf{k}}^{cv}}{(\xi_{\mathbf{k}+\mathbf{M}}^c - \xi_{\mathbf{k}}^v)(f_{\mathbf{k}+\mathbf{M},c} - f_{\mathbf{k},v})} \times \sum_{\mathbf{q}, \nu} \left[\sum_{\nu_2} I(\xi_{\mathbf{k}+\mathbf{q}}^{\nu_2}, \xi_{\mathbf{k}}^v, \Omega_{\mathbf{q}\nu}) |g_{\nu_2 \nu \nu}(\mathbf{k}, \mathbf{q})|^2 + \sum_{c_2} I(\xi_{\mathbf{k}+\mathbf{M}+\mathbf{q}}^{c_2}, \xi_{\mathbf{k}+\mathbf{M}}^c, \Omega_{\mathbf{q}\nu}) |g_{c_2 c \nu}(\mathbf{k} + \mathbf{M}, \mathbf{q})|^2 \right] \equiv -Z_{\mathbf{k}}^{cv} \Delta_{\mathbf{k}}^{cv}. \quad (56)$$

By adding Eq. (56) to the right-hand side of Eq. (45b), the gap equation is then modified by an overall ratio from the mass renormalization term:

$$\Delta_{\mathbf{k}}^{cv} \equiv \lambda_{\mathbf{k}}^{cv} g_{c\nu v_0}(\mathbf{k}, \mathbf{M}) (\chi_{b, \mathbf{M}v_0} + \chi_{b, \mathbf{M}v_0}^*), \quad (57)$$

where $\lambda_{\mathbf{k}}^{cv} = 1/(1 + Z_{\mathbf{k}}^{cv})$. Due to the occupation difference in the denominator, $Z_{\mathbf{k}}$ diverges and suppresses the potential $\Delta_{\mathbf{k}}$ for pairing between electron-electron ($e-e$) and hole-hole ($h-h$), such that the remaining configuration can only contain one electron and one hole ($e-h$ pairing).

In summary, Eq. (51) and Eq. (57) determine the gap that characterizes the excitonic insulator, which is induced by the e -ph coupling in a distorted lattice structure. The derived results contain the essential mass renormalization factors for the electronic and atomic sectors, which are absent in the conventional MF approach.

D. Gap equation due to Coulomb interaction

The third column of Fig. 2 contribute to the gap equation due to the Coulomb interaction. For Fig. 2(f), we can write

$$U^{(f)} = \sum_{c_1 v_1 c_2 v_2, \mathbf{k}, \mathbf{q}} \chi_{\mathbf{k}}^{c_1 v_1 *} \chi_{\mathbf{k}+\mathbf{M}-\mathbf{q}}^{c_2 v_2} W_{c_1 c_2 v_2 v_1}^{\mathbf{M}}(\mathbf{k}, \mathbf{q}), \quad (58)$$

where the screened Coulomb interaction $W^{\mathbf{M}}$ is in a general form and subjects to all approaches adopted in different numerical calculations. On the other hand, in Sec. IV, we will use the static limit for the screened Coulomb interaction for simplicity:

$$W_{c_1 c_2 v_2 v_1}^{\mathbf{M}}(\mathbf{k}, \mathbf{q}) = \sum_{\mathbf{G}, \mathbf{G}'} \frac{\epsilon_{\mathbf{G}\mathbf{G}'}^{-1}(\mathbf{q}) \rho_{v_1 v_2}^{\mathbf{G}}(\mathbf{k}, \mathbf{q}) \rho_{c_1 c_2}^{\mathbf{G}'*}(\mathbf{k} + \mathbf{M}, \mathbf{q})}{|\mathbf{q} + \mathbf{G}| |\mathbf{q} + \mathbf{G}'|}, \quad (59)$$

with the dipole element:

$$\rho_{nm}^{\mathbf{G}}(\mathbf{k}, \mathbf{q}) = \sum_{\mathbf{G}_1} u_{n\mathbf{k}}^{\mathbf{G}_1} u_{m\mathbf{k}}^{\mathbf{G} - \mathbf{G}_1}, \quad (60)$$

where the $u_{n\mathbf{k}}^{\mathbf{G}}$ is the periodic part of Bloch wave function in momentum space. In practice, we restrict to RPA-type Coulomb screening and ignore the quenching effect due to the band deformation in the ordered phase [101]. This assumption is available for determining the T_c since at the critical point the band deformation is infinitesimal. Below the T_c , how the quenching effect modifies the exciton condensation is presented in Refs. [60,61].

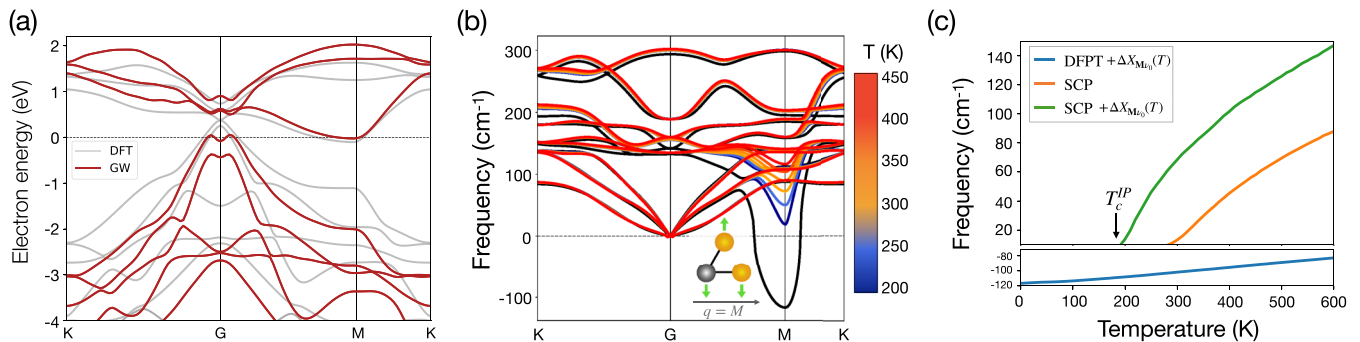


FIG. 3. (a) Band structure of monolayer TiSe₂ in disordered phase computed in DFT (gray) and the GW approximation (deep red) with spin-orbit coupling included. The electron pocket at the M point and the hole pocket at the Γ point shrink after the GW correction included. (b) The temperature dependence of the SCP phonon dispersion is encoded by the color map. The black line is computed by DFPT in the harmonic approximation, for which the appearance of the soft mode at the M point indicates the instability of the crystal structure against the formation of 2×2 CDW at zero temperature. Inset: The normal vibration mode of the soft mode at the M point. (c) Temperature-dependent phonon frequency of the soft mode at $\mathbf{q} = \mathbf{M}$. The blue line represents the frequency obtained from DFPT and corrected by the Coulomb-screened self-energy [Eqs. (28) and (29)]. The orange line represents the frequency obtained from the SCP theory with anharmonic effect included [Eqs. (31) and (32)]. The green line represents the frequency obtained from the SCP theory along with the Coulomb screened self-energy [Eq. (42)]. Since the green line denotes the fully renormalized phonon frequency without exciton correlation, it indicates a phase transition at $T_c^{IP} = 190$ K where lattice distorts due to phonon softening in independent particle (IP) approximation. When calculating the gap equation of exciton condensation, we adopt the fully renormalized phonon frequency to correct the e -ph coupling by Eq. (43).

On the other hand, Fig. 2(g) is the local Hartree potential from the anomalous density and can be written as

$$U^{(g)} = - \sum_{v_1 c_1 c_2 v_2, \mathbf{k}, \mathbf{k}'} \chi_{\mathbf{k}}^{c_1 v_1*} \chi_{\mathbf{k}'}^{c_2 v_2} v_{c_1 v_1 v_2 c_2}^{\mathbf{M}}(\mathbf{k}, \mathbf{k}'), \quad (61)$$

where

$$v_{c_1 v_1 v_2 c_2}^{\mathbf{M}}(\mathbf{k}, \mathbf{k}') = \sum_{\mathbf{G}} \frac{\rho_{v_2 c_2}^{\mathbf{G}*}(\mathbf{k}', \mathbf{M}) \rho_{v_1 c_1}^{\mathbf{G}}(\mathbf{k}, \mathbf{M})}{|\mathbf{M} + \mathbf{G}|^2}. \quad (62)$$

Combining the two diagrams and taking the derivative, we can obtain:

$$\begin{aligned} \frac{\partial U^{(f+g)}}{\partial \chi_{\mathbf{k}}^{c v}} &= \sum_{c_1 v_1, \mathbf{q}} \chi_{\mathbf{k}-\mathbf{M}+\mathbf{q}}^{c_1 v_1*} W_{c_1 c v v_1}^{\mathbf{M}}(\mathbf{k} - \mathbf{M} + \mathbf{q}, \mathbf{q}) \\ &\quad - \sum_{c_1 v_1, \mathbf{k}'} \chi_{\mathbf{k}'}^{c_1 v_1*} v_{c_1 v_1 v c}^{\mathbf{M}}(\mathbf{k}', \mathbf{k}), \end{aligned} \quad (63)$$

which will contribute to the right-hand side of Eq. (45b) when we include the Coulomb interaction to compute the gap equation. Equation (63) is not restricted to $\mathbf{q} = \mathbf{M}$ but for band mixing between states of general momentum pairing, \mathbf{k} and $\mathbf{k} + \mathbf{q}$. For the special case with $\mathbf{q} = 0$, Eq. (63) reduces to the gap equation derived in Ref. [62].

IV. EXCITON CONDENSATION IN MONOLAYER TiSe₂

This section presents the results for the EI/CDW phase in monolayer TiSe₂. Although the debate on the nature of the CDW in bulk TiSe₂ has been resolved by EEL experiments [27], a similar measurement for its monolayer crystal is still missing in the literature. Furthermore, current *ab initio* studies cannot incorporate electron and phonon coupling in a unified approach [46,57,102], and the e -h pairing mediated by phonon coupling has yet to be elucidated. Therefore, to

reveal the underlying mechanism of the unconventional CDW in monolayer TiSe₂, we apply the formalism developed in the last section to carry out numerical simulations of exciton condensation and discuss all the factors affecting the critical temperature from first principles.

A. Electronic structure of monolayer TiSe₂ in disordered phase

The first-principles electronic structure of monolayer TiSe₂ can be found in the literature [46], and here we present our calculation as a starting point. We perform the DFT calculation on the relaxed hexagonal structure using the QUANTUM ESPRESSO package [103], with the Perdew-Burke-Ernzerhof exchange-correlation functional and fully relativistic norm-conserving pseudopotentials generated with Pseudo Dojo [53,104,105]. Going beyond DFT, we use the VASP code to include the GW correction in an additional calculation [106]. All the computational details are summarized in Appendix F.

We present the computed DFT band structures along with GW correction in Fig. 3(a). To match the results, we align the Fermi level at 0 eV and connect isolated data points by the Wannier interpolation method using the interface between VASP and WANNIER90 [107]. Both DFT and GW calculations show that monolayer TiSe₂ is a semimetal, with a hole pocket near the Γ point and electron pocket in the M point while the Fermi surface is much smaller in the GW bands. By resolving the orbital in the band structure [46], we found that, with respect to the Fermi level, bands containing the Se p orbitals tend to be suppressed to lower energy while the bands with the Ti d orbitals can be promoted to higher energy in the GW correction. Near the Γ point, two kinds of orbital are entangled, leading to Mexican hatlike dispersions of the bands. Away from the Γ point, the overall vertical stretch between occupied and unoccupied bands is about 1 eV.

B. Temperature depending phonon dispersion

In bulk TiSe₂ a soft phonon with imaginary frequency has been observed and computed with wave vector $\mathbf{q} = L = (\frac{\pi}{2}, \frac{\pi}{2}, \frac{\pi}{2})$, which corresponds to the formation of $2 \times 2 \times 2$ CDW in three-dimensional crystal [33,108,109]. The soft phonon can be “hardened” by increasing the environment temperature. However, first-principles studies that used occupation broadening to simulate the finite-temperature effect showed that a substantial broadening is required for dynamical stability, leading to unrealistic high transition temperatures for both bulk and monolayer structures [46,108]. The failure of this approach indicates a strong anharmonicity in TiSe₂ beyond the harmonic approximation, which is highlighted in a recent study [102].

Here we apply the method introduced in Sec. II C to compute the self-consistent anharmonic phonon frequency and study the phonon softening in monolayer TiSe₂. In the practical procedure, we carry out the DFPT calculation using QUANTUM ESPRESSO to obtain the dynamical matrix and compute the e -ph matrix element with PERTURBO code [110]. We then use this matrix element in Eq. (26b) to compute the screened self-energy. To compute the phonon anharmonicity, we first use the *ab initio* molecular dynamics method implemented in VASP to generate the interatomic force and then compute the anharmonic phonon frequency by the ALAMODE code [65].

We present the temperature-dependent phonon dispersion in Fig. 3(b), where we plot the imaginary frequency in the minus axis. The black line represents a robust soft mode at the M point, which is the direct result of DFPT and is consistent with the formation of the 2×2 CDW in monolayer TiSe₂. The corresponding normal mode for the soft phonon is shown in the inset, which has an atomic displacement perpendicular to the wave vector. In the hexagonal Brillouin zone (BZ), there are three M points, and the condensation of these three normal modes can build up the lattice distortion observed in the CDW phase. Beyond the harmonic approximation, we observe that the soft phonon is the only mode sensitive to the anharmonic effect, while disregarding some temperature-independent correction. These results validate the single-mode assumption applied in Sec. III.

In Fig. 3(c), we analyze the soft-phonon at the M point. We present the phonon frequency as a function of temperature. We consider three different cases: (1) considering the correction only from the screening [Eqs. (28) and (29)], (2) considering the correction only from the anharmonic effect [Eqs. (31) and (32)], and (3) considering both the two effects [Eq. (42)]. First, we note that, at zero temperature, the harmonic DFPT gives us a phonon frequency $\omega_{\mathbf{M}}^{\text{DFPT}} = 116i \text{ cm}^{-1}$. When considering the temperature dependence in the Coulomb screened self-energy, the frequency varies by $30i \text{ cm}^{-1}$ from 0 K to 600 K (blue line), which indicates that the phonon will always be soft in the harmonic approximation. On the other hand, the pure anharmonic effect can raise the phonon frequency dramatically, forcing the phonon mode to become “hard” above $T = 270 \text{ K}$ (orange line). This critical temperature can even be reduced to $T = 190 \text{ K}$ when we combine the contribution from the two effects and solve the phonon frequency self-consistently (green line). In Fig. 4, we present the Coulomb screened self-energy with respect to its

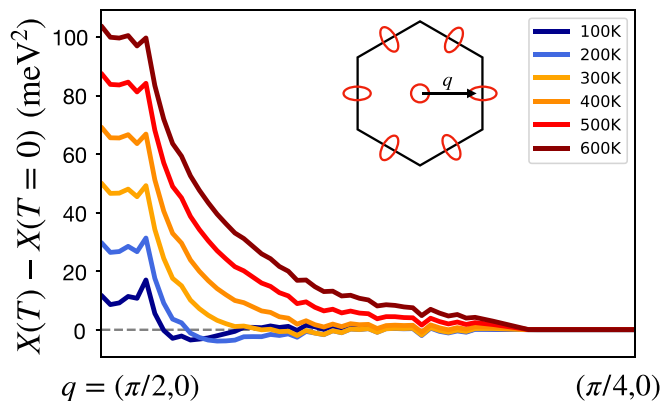


FIG. 4. Coulomb screened self-energy correction at finite temperature, Eq. (28), measured with respect to the zero-temperature value. Although the Fermi surface nesting is not significant (circle vs oval), remarkable temperature dependence can be found for phonon near $\mathbf{M} = (\pi/2, 0)$ connecting the electron packet and hole pocket.

zero-temperature value for phonon momentum \mathbf{q} along the high symmetry line $\text{M}-\Gamma$ under different temperatures. We note that the most significant temperature dependence does not occur for the momentum $\mathbf{q} = \mathbf{M}$ since the Fermi surface is not ideally “nesting.” Instead, it is approximately a constant for \mathbf{q} near the M point within a specific range and gradually decreases outside.

C. Gap equation

Based on the discussion in the last section, the EI/CDW lattice distortion is attributed to the combined effect of the three M phonons which requires to be treated explicitly. This “triple- \mathbf{q} ” effect requires us to extend the “single- \mathbf{q} ” formalism presented in Sec. III. More explicitly, we write the new wave function by introducing the pairing direction in Eq. (33):

$$\phi_{\mathbf{k}}^n = \sum_v t_{v\mathbf{k}}^n \psi_{v\mathbf{k}} + \sum_{c,I} t_{c\mathbf{k},I}^n \psi_{c\mathbf{k}+\mathbf{M}_I}, \quad (64)$$

where $I = 1, 2, 3$ is the index for the three \mathbf{M} directions. In a simplified two-band model, the mixing coefficients can be obtained by solving the triple- \mathbf{q} version of the Hamiltonian Eq. (39a):

$$\begin{pmatrix} \xi_{\mathbf{k}+\mathbf{M}_1}^c & 0 & 0 & \Delta_{\mathbf{k},1}^{cv} \\ 0 & \xi_{\mathbf{k}+\mathbf{M}_2}^c & 0 & \Delta_{\mathbf{k},2}^{cv} \\ 0 & 0 & \xi_{\mathbf{k}+\mathbf{M}_3}^c & \Delta_{\mathbf{k},3}^{cv} \\ \Delta_{\mathbf{k},1}^{vc} & \Delta_{\mathbf{k},2}^{vc} & \Delta_{\mathbf{k},3}^{vc} & \xi_{\mathbf{k}}^v \end{pmatrix} \begin{pmatrix} t_{c\mathbf{k},1}^n \\ t_{c\mathbf{k},2}^n \\ t_{c\mathbf{k},3}^n \\ t_{v\mathbf{k}}^n \end{pmatrix} = E_{n(\mathbf{k})} \begin{pmatrix} t_{c\mathbf{k},1}^n \\ t_{c\mathbf{k},2}^n \\ t_{c\mathbf{k},3}^n \\ t_{v\mathbf{k}}^n \end{pmatrix}, \quad (65)$$

where we neglect the pairing between states of $\mathbf{k} + \mathbf{M}_I$ and $\mathbf{k} + \mathbf{M}_J$ for which the momentum transfer exceeds the first BZ [111]. It can be shown that the effect of triple- \mathbf{q} will decouple from each other in the limit of $\Delta_{\mathbf{k}} \rightarrow 0$ and reduce to the single- \mathbf{q} scenario in the linear order as Eq. (55). This property reflects that the inclusion of the triple- \mathbf{q} effect only changes the finite $\Delta_{\mathbf{k}}$ behavior but maintains the critical temperature, T_c , where $\Delta_{\mathbf{k}} = 0$. The same extension is applicable to the gap equations when incorporating the triple- \mathbf{q} effect. Among all the expressions presented in Sec. III, we implement the

extension

$$\begin{aligned} (\Delta_b, \Delta_{\mathbf{k}}^{cv}, \chi_{b,\mathbf{M}}, \chi_{\mathbf{k}}^{cv}) &\rightarrow (\Delta_{b,I}, \Delta_{\mathbf{k},I}^{cv}, \chi_{b,\mathbf{M}_I}, \chi_{\mathbf{k},I}^{cv}) \\ (\lambda_b, \lambda_{\mathbf{k}}^{cv}, W^{\mathbf{M}}, v^{\mathbf{M}}) &\rightarrow (\lambda_{b,I}, \lambda_{\mathbf{k},I}^{cv}, W^{\mathbf{M}_I}, v^{\mathbf{M}_I}) \\ g_{cvv_0}(\mathbf{k}, \mathbf{M}) &\rightarrow g_{cvv_0}(\mathbf{k}, \mathbf{M}_I) \end{aligned} \quad (66)$$

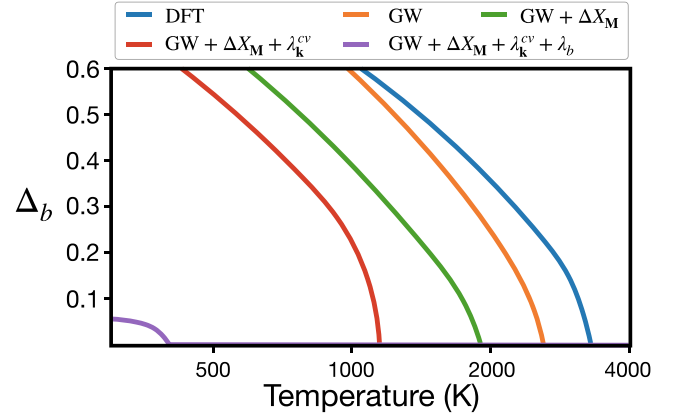
by introducing the I index to address the three directions comprehensively. In the rest of the section, we will self-consistently solve Eq. (65) of general $\Delta_{\mathbf{k},I}^{vc}$'s along with the extended gap equations to discuss the phase transition in monolayer TiSe_2 .

To comprehensively understand the role of each component in the gap equation, we note that the temperature dependence in the EI/CDW gap equations lies in electronic occupation, phonon frequency, electron-phonon coupling, and mass renormalization coefficients, and each factor is crucial to compute the critical temperature. To emphasize their importance, we first apply the MF gap equations, Eq. (45a) and Eq. (45b), as a baseline and use the DFT band structure with the phonon frequency near the experimental critical temperature, $T_c^{\text{exp.}} = 220$ K. However, the result yields an extreme high T_c , since the small frequency, $\Omega_{\mathbf{M}}(T_c^{\text{exp.}}) = 27.4 \text{ cm}^{-1}$, can boost the phonon thermal average with small potential Δ_b and enhance the coupling constant by Eq. (43). These two effects make the critical temperature higher than 10^6 K.

To analyze how the phonon frequency affects the critical temperature, we restrict discussions in the MF gap equation and study three different scenarios. First, we restore the temperature dependence in the anharmonic phonon frequency without correction on Coulomb screened self-energy [orange line in Fig. 3(c)]. A great improvement in the critical temperature is obtained (see blue line in Fig. 5), which gives $T_c \sim 3300$ K with the critical phonon frequency $\Omega_{\mathbf{M}}^c = 308 \text{ cm}^{-1}$. Compared to the fixed-frequency case, a 10-times enhancement on $\Omega_{\mathbf{M}}$ can suppress the critical temperature by three orders of magnitude. This modification reflects that in a BCS-like mean-field theory, $T_c \sim \exp(1/U)$, where the pairing potential U is characterized by $|g_{\mathbf{M}}^2|/\Omega_{\mathbf{M}}$ here [7,112].

Next we add the GW correction to increase the relative energy between occupied and unoccupied states. The result with a modified band structure differs from the calculation with DFT bands only at temperatures higher than 1200 K (see the orange line in Fig. 5); on the other hand, at temperatures lower than 1200 K, the coupling $\Delta_{\mathbf{k}}^{cv}$ is much larger than 1 eV, which makes the GW correction irrelevant. Last, fixed on the GW band, we use the phonon frequency dressed by the temperature-dependent polarization screening [green line in Fig. 3(c)], which can suppress the lattice distortion potential in the whole temperature ranges and lower the T_c to 1950 K. We found that although the T_c is significantly reduced, the critical frequency $\Omega_{\mathbf{M}}^c$ is merely changed (see the table in Fig. 5). Thus, we conclude that in the mean-field approach, the major temperature-dependent factor in EI/CDW phase transition is dominated by the phonon frequency; disregarding the temperature, as long as the phonon has a frequency lower than $\sim 275 \text{ cm}^{-1}$, the lattice structure becomes unstable and transit into the distorted 2×2 superlattice.

The critical frequency $\Omega_{\mathbf{M}}^c \sim 275 \text{ cm}^{-1}$ obtained above is extremely high, since the highest phonon mode in the full



Correction Types	Band structure	phonon frequency	mass renormalization	T_c (K)	$\Omega_{\mathbf{M}}^c$ (cm^{-1})
(not shown)	DFT	fixed at T=220 K	N/A	$>10^6$	27.4
— DFT	DFT	SCP	N/A	3300	308
— GW	GW	SCP	N/A	2650	275
— GW + $\Delta X_{\mathbf{M}}$	GW	SCP + $\Delta X_{\mathbf{M}_0}(T)$	N/A	1950	279
— GW + $\Delta X_{\mathbf{M}}$ + $\lambda_{\mathbf{k}}^{cv}$	GW	SCP + $\Delta X_{\mathbf{M}_0}(T)$	$\lambda_{\mathbf{k}}^{cv}$	1160	217
— GW + $\Delta X_{\mathbf{M}}$ + $\lambda_{\mathbf{k}}^{cv}$ + λ_b	GW	SCP + $\Delta X_{\mathbf{M}_0}(T)$	$\lambda_{\mathbf{k}}^{cv}, \lambda_b$	400	103

FIG. 5. Temperature depending phonon displacement potential computed under different corrections. The inclusion of the phonon mass renormalization term suppresses the potential in the whole temperature range, while other corrections provide a rigid shift. Table: Summaries of critical temperature and corresponding phonon frequency of each correction type.

dispersion is about 300 cm^{-1} [see Fig. 3(b)]. This indicates that using the MF gap equation is insufficient. In the following, we discuss the mass renormalization effect by considering Eq. (51) and Eq. (57) beyond the MF approach. In Fig. 6(a), we present the electron mass renormalization coefficient $\lambda_{\mathbf{k}}^{cv}$ as a function of energy transition. The result shows a symmetric pattern with respect to the zero-energy transition since we involve the same number of bands for states with wave vector \mathbf{k} and $\mathbf{k} + \mathbf{M}$; for each $v\mathbf{k}$ and $c\mathbf{k} + \mathbf{M}$, there is always a corresponding $v\mathbf{k} + \mathbf{M}$ and $c\mathbf{k} + 2\mathbf{M}$ which has the opposite energy difference. Overall, $\lambda_{\mathbf{k}}^{cv}$ can be categorized into three types. The first is the zero values ranging from -2.0 to 2.0 eV. They correspond to the mixing between bands below (h-h) or above ($e-e$) the Fermi level as discussed in Sec. III C. The second is the smooth change from 1.0 to 0.0 when $\xi_{\mathbf{k}+\mathbf{M}}^c - \xi_{\mathbf{k}}^v$ approaches zero. This behavior is controlled by the divergence of $Z_{\mathbf{k}}^{cv}$ due to the energy difference term in the denominator in Eq. (56). It should be noted that for cases with small $\xi_{\mathbf{k}+\mathbf{M}}^c - \xi_{\mathbf{k}}^v$ the vanishing $\lambda_{\mathbf{k}}^{cv}$ will not forbid the pairing as long as occupation difference $f_{\mathbf{k}+\mathbf{M},c} - f_{\mathbf{k},v}$ is finite. Taking Eq. (65) as an example, although the pairing potential $\Delta_{\mathbf{k}}^{cv}$ is weak in this scenario, the relative spacing among diagonal terms $\xi_{\mathbf{k}}^i$ is also small such that the resultant eigenvector $t_{i\mathbf{k}}^n$ can still create a significant pairing effect. The third is the vertical scattered distribution near $\xi_{\mathbf{k}+\mathbf{M}}^c - \xi_{\mathbf{k}}^v \approx \pm 2.0$ eV which is the intermediate type of the previous two. $\lambda_{\mathbf{k}}^{cv}$ of this kind comes

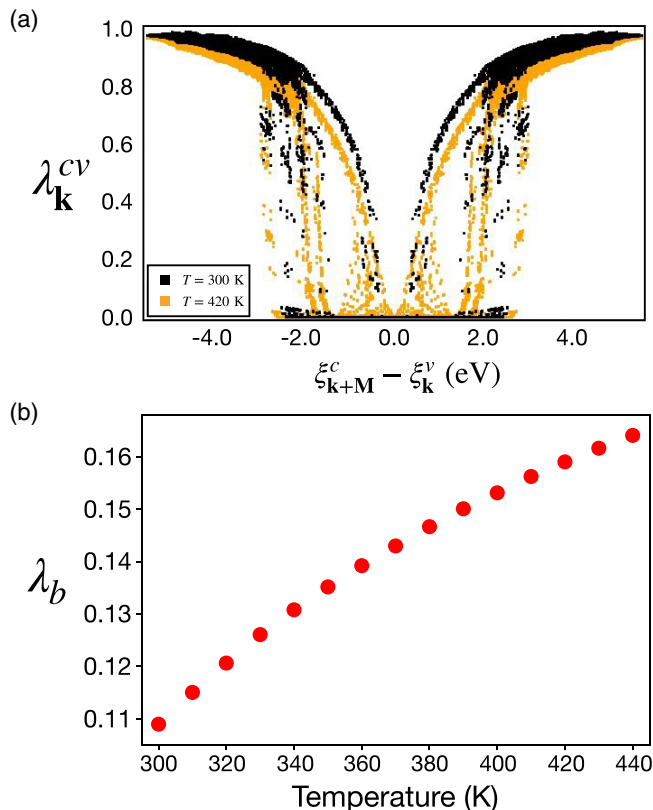


FIG. 6. Mass renormalization coefficients near the critical temperature. (a) The exciton condensation mass renormalization coefficients can be categorized into three kinds: those coming from the e - e (h - h) pairing, energy modulation, and pairing involving states near the Fermi surface, respectively. The overall values decrease when temperature rises. (b) Phonon displacement mass renormalization coefficient increases along with temperature.

from the pairing involving states near the Fermi-surface where the pairing configuration can easily change from e - h to e - e or h - h pairing and reduce the $\lambda_{\mathbf{k}}^{cv}$ within a small energy variation. Overall, Fig. 6(a) shows that raising the temperature from $T = 300$ K to $T = 420$ K decreases $\lambda_{\mathbf{k}}^{cv}$ and weakens the pairing potential, thereby accelerating the onset of the critical temperature during heating. Conversely, Fig. 6(b) illustrates the behavior of the mass renormalization coefficient λ_b from the phonon sector, which increases with temperature. The result is in the opposite trend from the $\lambda_{\mathbf{k}}^{cv}$'s because the \mathcal{Z}_b factor is inversely proportional to the phonon frequency such that smaller Ω_M can result in a smaller λ_b and vice versa.

To examine the renormalization effect, we work out the renormalized gap equation, Eq. (51) and Eq. (57), with the computed coefficients $\lambda_{\mathbf{k}}^{cv}$ but keeping $\lambda_b = 1$. The corresponding gap function is presented as the red line in Fig. 5. Compared with the MF result (green line), for $\Delta_b > 0.3$, $\lambda_{\mathbf{k}}^{cv}$ contributes a rigid shift lowering the Δ_b by 0.1 while, for $\Delta_b < 0.3$, Δ_b becomes unstable and drop to zero within $\Delta T = 200$ K, such that the critical temperature is reduced by ~ 800 K, and the character of second-order transition becomes more significant [113]. Next, we turn on the λ_b and obtain the fully renormalized gap function (purple line in Fig. 5). Besides reducing the critical temperature, λ_b modifies the atom

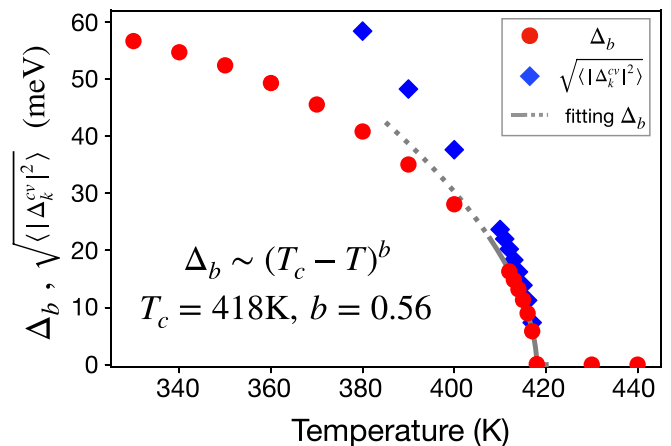


FIG. 7. EI/CDW potential calculated from first principles. The computed critical temperature is $T_c = 418$ K while the experimental measure is $T_c^{\text{exp}} = 220$ K. The fitted critical component $b = 0.56$ is in great agreement with the square root trend in the experiment [48].

displacement potential within the EI/CDW phase. Without λ_b , Δ_b will blow up exponentially as temperature decreases, but λ_b can significantly suppress the Δ_b at a lower temperature. So that the $\Delta_b - T$ curve becomes flat except near the critical temperature. Now, at the critical temperature, $T_c = 400$ K, the corresponding critical frequency $\Omega_M^c = 103$ cm^{-1} which is comparable to the folded phonon frequency computed at Γ point $\Omega_{M \rightarrow \Gamma} \sim 75$ cm^{-1} in the 2×2 CDW phase [46].

Last, to include all factors that could affect the T_c , we restore the e - h Coulomb attraction into the gap equation by using Eq. (63) where the screened Coulomb matrix elements are extracted using the BSE subroutine in the YAMBO codes [114]. We present the result as one of the main conclusions in this work in Fig. 7, where we plot the distortion potential Δ_b along with the averaged e - h pairing potential, $\sqrt{\langle |\Delta_{\mathbf{k}}^{cv}|^2 \rangle}$. The inclusion of the Coulomb force only raises the critical temperature by 20 K. We note that with the Coulomb attraction as the only mechanism in the MF approach, the critical temperature is ~ 600 K, much lower than the $T_c = 1950$ by e - ph coupling. Besides, the Coulomb kernel is restricted to pairing near the Fermi surface, which is thus easier to be restrained by the mass renormalization factor. Therefore, we conclude that the underlying mechanism causing the formation of the CDW order in monolayer TiSe_2 is the strong electron-phonon coupling mixing the occupied and unoccupied states. At the same time, the screened Coulomb attraction can only provide a minor contribution λ during the phase transition. Fitting the discrete data near the critical point, we obtain the critical temperature $T_c = 418$ K with a critical component $b = 0.56$ in the temperature dependence $\Delta_b \sim (T_c - T)^b$, which is consistent with the experimental observation [48].

D. Discussion

Before concluding, we make some remarks regarding the comparison of theoretical calculations and real material measurements. First, we note that in a two-dimensional system, the Mermin-Wagner theorem [115] states that there can be no phase transition due to continuous symmetry breaking,

and, instead, a Kosterlitz-Thouless transition occurs for the formation of quasi-long-range ordering [116], which makes a BCS-like MF approach overestimate the critical temperature of a 2D phase transition. Consequently, some criticisms may arise regarding the applicability of our approach to two-dimensional systems, considering the Mermin-Wagner theorem. However, it is pertinent to emphasize that the no-go theorem imposed by Mermin and Wagner does not apply for the EI/CDW transition in monolayer TiSe₂. This distinction is demonstrated in the work of Kohn *et al.* [117], where they establish that, in a general exciton condensation, only a diagonal long-range order is feasible for the formation of a charge-density wave, but no continuous symmetry breaking occurs [118,119] [120]. Furthermore, the experiment [48] indeed observed a BCS-like transition, allowing us to apply a mean-field-like approach without considering the Kosterlitz-Thouless transition. Overall, these insights underscore the robustness of our approach and provide a basis for further investigating the intriguing properties of two-dimensional systems.

Another factor that needs to be considered is the presence of synthesized defects at the Se site or charge transfer from the substrate, which can cause a finite electron-doping effect in experimental measurements. In bulk, this effect is found to reduce the T_c of CDW [121], and anharmonic calculations suggest the same effect for the monolayer [102]. We want to emphasize that the methodology presented in this work is capable of producing the same trend when taking into account electron-doping at each numerical step, as summarized in Fig. 1. However, since a nondoped sample can be obtained through exfoliation [122] and the computation cost for the DFPT and anharmonicity calculation in a doped system is too heavy, we will leave the detailed study of the doping effect for future work.

V. CONCLUSION

In this work, we have presented a *ab initio* approach that extends DFT to describe structural phase transitions caused by exciton condensation. Our approach introduces the nonlocal density to encode the spontaneous formation of exciton pairs by Coulomb attraction and *e-ph* interaction. We also included phonon anharmonicity in the phonon sector by using self-consistent phonon theory to harden the soft-phonon appearing in DFPT. In addition, we bring in a linear distortion potential to measure the lattice deformation. The exchange-correlation function in this generalized DFT can be computed by the many-body perturbation theory with the assistance of the linked-cluster expansion such that a gap equation to describe the EI/CDW can be derived self-consistently.

In practical application, we use the formalism to study the 1T-TiSe₂ monolayer crystal. The numerical results favor our method over the mean-field approach by crucial mass renormalization effects in both electron and phonon states. We obtained a second-order phase transition between a semimetal and a 2×2 CDW caused by *e-ph* coupling with critical temperature $T_c = 420$ K compared to the experimental value of 220 K. Compared to the standard anharmonic phonon calculation, our results present a lattice distortion at the temperature region without phonon softening.

To the best of our knowledge, this work is the first *ab initio* study that analyzes the role of ph-ph, *e-ph*, and *e-e* interactions on the same footing for TiSe₂. Our work provides a framework for predicting exciton condensation and studying its relation to lattice instability from first principles, and the methodology can be generalized to other excitonic insulators beyond the example studied in this work. These calculations can guide the future search for candidate material with the excitonic insulating phase.

ACKNOWLEDGMENTS

We are grateful for fruitful discussions with A. S. Mishchenko and R. Masuki. We acknowledge the financial support by Grant-in-Aids for Scientific Research (JSPS KAKENHI) (Grant No. JP19H05825), JST PRESTO (Grant No. JPMJPR20L7), and “Program for Promoting Researches on the Supercomputer Fugaku” (Project ID: hp220166) from MEXT, Japan.

APPENDIX A: GW CORRECTION FROM NL DENSITY

Here we use Eq. (19) to derive the correction due to the NL XC potential $\hat{\Delta}_{XC}$ and show the agreement between this approach and the GW correction. Based on the assumption of GWA that the XC potential can be diagonalized by the KS wave function, we can identify the function of Eq. (14) and Eq. (16) such that $\phi_n(\mathbf{r}) = \psi_n(\mathbf{r})$ and the second line in Eq. (16) becomes

$$\begin{aligned} & \int d^3\mathbf{r}d^3\mathbf{r}'\psi_n^*(\mathbf{r})[\Delta_{xc}(\mathbf{r},\mathbf{r}') - \delta(\mathbf{r}-\mathbf{r}')v_{xc}(\mathbf{r})]\psi_m(\mathbf{r}') \\ & \equiv \delta_{nm}(\Delta_n - \langle n|v_{xc}|m \rangle), \end{aligned} \quad (A1)$$

which provides a linear correction on KS eigenenergy:

$$E_n = \xi^n + \Delta_n - \langle n|v_{xc}|n \rangle. \quad (A2)$$

To evaluate the NL XC potential, we consider the Feynman diagram in Fig. 2(f). To be consistent with GWA, unlike the static approximation adopted in the main text, we consider the dynamical screening here. In the periodic system, we utilize the Bloch wave function:

$$\psi_n(\mathbf{r}) \rightarrow \psi_{n\mathbf{k}}(\mathbf{r}) = \sum_{\mathbf{G}} u_{n\mathbf{k}}^{\mathbf{G}} e^{i(\mathbf{G}+\mathbf{k})\mathbf{r}}, \quad (A3)$$

where \mathbf{G} is the unit vector in reciprocal lattice. Thus, we are able to write the Green's function using the Matsubara representation for a thermal system:

$$\begin{aligned} G(\mathbf{r},\mathbf{r}';\omega_n) &= - \int_0^\beta d\tau e^{i\omega_n\tau} \langle \mathcal{T} \Psi(\mathbf{r},\tau) \Psi^\dagger(\mathbf{r}',0) \rangle \\ &= \sum_{n\mathbf{k}} \frac{\psi_{n\mathbf{k}}(\mathbf{r})\psi_{n\mathbf{k}}^*(\mathbf{r}')}{i\omega_n - E_{n\mathbf{k}}} = \sum_{n\mathbf{k}} G_{n\mathbf{k}}(\mathbf{r},\mathbf{r}';\omega_n) \end{aligned} \quad (A4)$$

with $\omega_n = (2n + 1)\pi/\beta$ being the Matsubara frequency. And we can compute the diagram by the Feynman rule:

$$\begin{aligned} U^{(f)} &= \sum_{\substack{n,m,\mathbf{k},\mathbf{q} \\ \omega_n, \nu_n}} \int d^3\mathbf{r}d^3\mathbf{r}' W(\mathbf{q}, \nu_n - \omega_n, \mathbf{r}', \mathbf{r}) \\ &\quad \times G_{m\mathbf{k}-\mathbf{q}}(\mathbf{r}, \mathbf{r}'; \omega_n) G_{n\mathbf{k}}(\mathbf{r}', \mathbf{r}; \nu_n) \\ &= \sum \frac{\epsilon_{\mathbf{G}\mathbf{G}'}^{-1}(\mathbf{q}, \omega_n - \nu_n) \rho_{nm}^{\mathbf{G}}(\mathbf{k}, \mathbf{q}) \rho_{nm}^{\mathbf{G}'*}(\mathbf{k}, \mathbf{q})}{(i\omega_n - E_{n\mathbf{k}})(i\nu_n - E_{m\mathbf{k}-\mathbf{q}}) |\mathbf{q} + \mathbf{G}| |\mathbf{q} + \mathbf{G}'|}. \end{aligned} \quad (\text{A5})$$

The dynamical Coulomb screening can be approximated by the plasmon pole approximation (PPA) [80,123,124] as

$$\begin{aligned} \epsilon_{\mathbf{G}\mathbf{G}'}^{-1}(\mathbf{q}, \omega) &\approx \delta_{\mathbf{G}\mathbf{G}'} + \mathbf{R}_{\mathbf{q},\mathbf{G}\mathbf{G}'} \\ &\quad \times \left[\frac{1}{\omega - \Omega_{\mathbf{q},\mathbf{G}\mathbf{G}'} + i0^+} - \frac{1}{\omega + \Omega_{\mathbf{q},\mathbf{G}\mathbf{G}'} - i0^+} \right], \end{aligned} \quad (\text{A6})$$

where the residue $\mathbf{R}_{\mathbf{q},\mathbf{G}\mathbf{G}'}$ and the effective plasmon frequency can be obtained by fitting Eq. (A6) with the real dielectric constant computed at $\omega = 0$ and a chosen PPA imaginary frequency $\omega = i\omega_p$ [123]. By summing the Matsubara frequency, we can obtain:

$$\begin{aligned} U^{(f)} &= \sum_{\mathbf{G}\mathbf{G}'\mathbf{q}\mathbf{m}\mathbf{m}} \frac{\rho_{nm}^{\mathbf{G}}(\mathbf{k}, \mathbf{q}) \rho_{nm}^{\mathbf{G}'*}(\mathbf{k}, \mathbf{q})}{|\mathbf{q} + \mathbf{G}| |\mathbf{q} + \mathbf{G}'|} \left\{ \delta_{\mathbf{G},\mathbf{G}'} f_{\mathbf{k},n} f_{\mathbf{k}-\mathbf{q},m} \right. \\ &\quad - \mathbf{R}_{\mathbf{q},\mathbf{G}\mathbf{G}'} \left[\frac{f_{\mathbf{k},n} f_{\mathbf{k}-\mathbf{q},m} + f_{\mathbf{k}-\mathbf{q},m} \mathcal{N}_{\mathbf{q},\mathbf{G}\mathbf{G}'}^+ + f_{\mathbf{k},n} \mathcal{N}_{\mathbf{q},\mathbf{G}\mathbf{G}'}^-}{\Omega_{\mathbf{q},\mathbf{G}\mathbf{G}'} - E_{n\mathbf{k}} + E_{m\mathbf{k}-\mathbf{q}}} \right] \\ &\quad \left. + \mathbf{R}_{\mathbf{q},\mathbf{G}\mathbf{G}'} \left[\frac{f_{\mathbf{k},n} f_{\mathbf{k}-\mathbf{q},m} + f_{\mathbf{k}-\mathbf{q},m} \mathcal{N}_{\mathbf{q},\mathbf{G}\mathbf{G}'}^- + f_{\mathbf{k},n} \mathcal{N}_{\mathbf{q},\mathbf{G}\mathbf{G}'}^+}{-\Omega_{\mathbf{q},\mathbf{G}\mathbf{G}'} - E_{n\mathbf{k}} + E_{m\mathbf{k}-\mathbf{q}}} \right] \right\}. \end{aligned} \quad (\text{A7})$$

where we use the shorthand $\mathcal{N}_{\mathbf{q},\mathbf{G}\mathbf{G}'}^{\pm}$ for the bosonic occupation $n_B(\pm\Omega_{\mathbf{q},\mathbf{G}\mathbf{G}'})$. In the limit when the dielectric tensor contains only diagonal term and no frequency dependence, i.e., $\mathbf{R}_{\mathbf{q},\mathbf{G}\mathbf{G}'} = 0$, Eq. (A7) reduces to the case without dynamical screening derived in Ref. [64]. Based on the fact that $\chi_{\mathbf{k}}^m = f_{n\mathbf{k}}$ when $\phi_n(\mathbf{r}) = \psi_n(\mathbf{r})$, we can take the derivative on Eq. (A7) and obtain the energy correction from the NL potential:

$$\begin{aligned} \Delta_{n\mathbf{k}} &= \sum_{\mathbf{G}\mathbf{G}'\mathbf{q}\mathbf{m}} \frac{\rho_{nm}^{\mathbf{G}}(\mathbf{k}, \mathbf{q}) \rho_{nm}^{\mathbf{G}'*}(\mathbf{k}, \mathbf{q})}{|\mathbf{q} + \mathbf{G}| |\mathbf{q} + \mathbf{G}'|} \\ &\quad \times \left\{ f_{\mathbf{k}-\mathbf{q},m} \left[\delta_{\mathbf{G},\mathbf{G}'} + \frac{2\Omega_{\mathbf{q},\mathbf{G}\mathbf{G}'} \mathbf{R}_{\mathbf{q},\mathbf{G}\mathbf{G}'}}{(E_{n\mathbf{k}} - E_{m\mathbf{k}-\mathbf{q}})^2 - \Omega_{\mathbf{q},\mathbf{G}\mathbf{G}'}^2} \right] \right. \\ &\quad \left. + \mathbf{R}_{\mathbf{q},\mathbf{G}\mathbf{G}'} \left[\frac{\mathcal{N}_{\mathbf{q},\mathbf{G}\mathbf{G}'}^-}{-\Omega_{\mathbf{q},\mathbf{G}\mathbf{G}'} + E_{n\mathbf{k}} - E_{m\mathbf{k}-\mathbf{q}}} - (\Omega \rightarrow -\Omega) \right] \right\}. \end{aligned} \quad (\text{A8})$$

Consequently, Eq. (A2) and Eq. (A8) reproduce the GW correction [80,125] where in Eq. (A8) the first occupation depending term gives the screened exchange part, Σ_{SEX} , while the second term produces the electron-hole part Σ_{COH} [126].

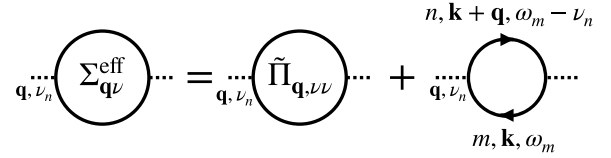


FIG. 8. The phonon self-energy diagrams due to the interacting term, Eq. (39b) where n, m are the band index for the electron loops and ω_m and ν_n are the Matsubara frequency of electron and phonon, respectively.

APPENDIX B: DRESSED PHONON FREQUENCY IN EFFECTIVE HAMILTONIAN EQ. (39a) AND EQ. (39b)

Here we present the detail to derive the renormalized phonon frequency in the diagonal approximation, Eq. (42), based on the unperturbed Hamiltonian Eq. (39a) under the effect of interacting Hamiltonian Eq. (39b). In terms of Feynman's diagram, the lowest-order phonon self-energy can be presented by the one-particle irreducible Feynman's diagrams as in Fig. 8 where the first diagram is the effective term from anharmonic ph-ph interaction subtracted by the screened part at zero temperature, and the second term is the contribution from the screening effect at finite temperature.

Using the Feynman rule, the effective self-energy can be written as

$$\begin{aligned} \Sigma_{\mathbf{q}\nu}^{\text{eff}}(i\nu_n) &= \tilde{\Pi}_{\mathbf{q},\nu\nu} + 2 \sum_{nm,\mathbf{k}\omega_m} |g_{nm\nu}^{\text{DFPT}}(\mathbf{k}, \mathbf{q})|^2 \\ &\quad \times \frac{1}{i\omega_m - \xi_{\mathbf{k}}^m} \frac{1}{i(\omega_m - \nu_n) - \xi_{\mathbf{k}+\mathbf{q}}^n}, \end{aligned} \quad (\text{B1})$$

where the factor of two in the second line appears to take into account the spin degree of freedom. Summing over the Matsubara frequency and taking the analytical continuation to a negligible phonon frequency $i\nu_n \rightarrow \omega_{\mathbf{q}\nu} \approx 0$, we can obtain

$$\Sigma_{\mathbf{q}\nu}^{\text{eff}} = \tilde{\Pi}_{\mathbf{q},\nu\nu} + \frac{X_{\mathbf{q}\nu}(T)}{\omega_{\mathbf{q}\nu}^{\text{DFPT}}}. \quad (\text{B2})$$

Therefore, the dressed phonon frequency becomes Eq. (42)

$$\begin{aligned} \Omega_{\mathbf{q}\nu}^2 &= \omega_{\mathbf{q}\nu}^{\text{DFPT}2} + 2\omega_{\mathbf{q}\nu}^{\text{DFPT}} \Sigma_{\mathbf{q}\nu}^{\text{eff}} \\ &= \omega_{\mathbf{q}\nu}^{\text{DFPT}2} + 2X_{\mathbf{q}\nu}(T) \Big|_{T=0} + 2\Omega_{\mathbf{q}\nu} \Sigma_{\mathbf{q}\nu}(T), \end{aligned} \quad (\text{B3})$$

which is designed to be consistent with the phonon frequency computed by SCP theory.

APPENDIX C: ONE-DIMENSIONAL TWO-BAND MODEL

In this Appendix, we work out the MF gap equations Eq. (45a) and Eq. (45b) in the most simplified case in one-dimensional system with two isolated bands and present the connection between our formalism and the approach introduced in Ref. [9] and Ref. [62]. By focusing on a single transition momentum $q = M = \pi/2$, the system can be

described by a reduced Hamiltonian:

$$H = \sum_k \xi_k^c \hat{c}_k^\dagger \hat{c}_k + \xi_k^v \hat{f}_k^\dagger \hat{f}_k + \Omega \hat{b}_M^\dagger \hat{b}_M + \sum_k (g_k \hat{c}_{k+M}^\dagger \hat{f}_k + \text{H.c.}) (\hat{b}_{-M}^\dagger + \hat{b}_M), \quad (\text{C1})$$

where we consider only one vibration mode and keep e -ph interaction for phonon with momentum $q = M$. g_k is the e -ph matrix element describing the scattering between holes in an occupied state f and electrons in an unoccupied state c by phonon exchanging. In the exciton condensation phase, the electron and hole operator acquires a finite thermal expectation value, $\langle \hat{c}_{k+M}^\dagger \hat{f}_k \rangle$, accompanied by a finite $\langle \hat{b}_M \rangle$ for phonon operator such that the electronic ground state becomes unstable and atoms distort from their equilibrium position. Following the procedure introduced in the main text, we first work on Eq. (39a) by solving the eigenvalue problem:

$$\begin{pmatrix} \xi_{k+M}^c & \Delta_k^{cv} \\ \Delta_k^{vc} & \xi_k^v \end{pmatrix} \begin{pmatrix} t_{ck}^n \\ t_{vk}^n \end{pmatrix} = E_{n(k)} \begin{pmatrix} t_{ck}^n \\ t_{vk}^n \end{pmatrix}, \quad (\text{C2})$$

which gives the eigenenergy:

$$E_{\pm k} = \frac{\xi_{k+M}^c + \xi_k^v}{2} \pm W_k \quad (\text{C3})$$

and eigenvectors:

$$t_{ck}^+ = \frac{e^{i\theta_k}}{\sqrt{2}} \sqrt{1 + \frac{\xi_{k+M}^c - \xi_k^v}{2W_k}}, \quad t_{vk}^+ = \frac{1}{\sqrt{2}} \sqrt{1 - \frac{\xi_{k+M}^c - \xi_k^v}{2W_k}}$$

$$t_{ck}^- = \frac{-1}{\sqrt{2}} \sqrt{1 - \frac{\xi_{k+M}^c - \xi_k^v}{2W_k}}, \quad t_{vk}^- = \frac{e^{-i\theta_k}}{\sqrt{2}} \sqrt{1 + \frac{\xi_{k+M}^c - \xi_k^v}{2W_k}}, \quad (\text{C4})$$

where

$$W_k = \sqrt{\left(\frac{\xi_{k+M}^c - \xi_k^v}{2}\right)^2 + |\Delta_k^{cv}|^2}, \quad \theta_k = \arg(\Delta_k^{cv}). \quad (\text{C5})$$

Based on the solution, we can write the NL density as follows:

$$\chi_k^{cv} = t_{ck}^{+*} t_{vk}^+ f_{k,+} + t_{ck}^{-*} t_{vk}^- f_{k,-} = \frac{\Delta_k^{cv*}}{2W_k} (f_{k,+} - f_{k,-}). \quad (\text{C6})$$

On the other hand, for the phonon, we take the result, Eq. (D2) from the next section:

$$\chi_b = \langle b_M \rangle = \frac{-\Delta_b}{\Omega}. \quad (\text{C7})$$

As a result, using Eq. (C6) and Eq. (C7) for Eq. (45a) and Eq. (45b), we can obtain the gap function:

$$1 = \sum_k \frac{2|g_k|^2}{\Omega} \frac{f_{k,-} - f_{k,+}}{W_k}, \quad (\text{C8})$$

which reduces to the result in Ref. [9] when we neglect the momentum dependence in e -ph coupling by taking $g_k \equiv g$.

Last, to compare with the BSE approach presented in Ref. [62], we apply Eq. (C6) to Eq. (63) and replace the M

transition by the vertical Γ transition such that we obtained

$$\frac{\partial U^{(f+g)}}{\partial \chi_k} = \sum_{\mathbf{k}'} \chi_{\mathbf{k}'}^* [W_{c'v'v}(\mathbf{k}', \mathbf{k}' - \mathbf{k}) - v_{c'v'v}(\mathbf{k}', \mathbf{k})]. \quad (\text{C9})$$

By simplifying the expression with $\tilde{W}(\mathbf{k}', \mathbf{k}) = v - W$, we can add Eq. (C9) to the right-hand side of Eq. (45b) and turn-off the e -ph coupling, such that, at 0 K, the gap equation becomes

$$\Delta_{\mathbf{k}} = \sum_{\mathbf{k}'} \frac{\Delta_{\mathbf{k}'}}{2W_{\mathbf{k}'}} \tilde{W}(\mathbf{k}', \mathbf{k}). \quad (\text{C10})$$

Using the notation, $\varphi_{\mathbf{k}} = \frac{\Delta_{\mathbf{k}}}{2W_{\mathbf{k}}}$, we can recover the Eq. (33) in the supplementary material of Ref. [62].

APPENDIX D: PHONON GREEN'S FUNCTION WITH DISPLACEMENT POTENTIAL

In this section, we derive the phonon Green's function when the phonon operator is applied by an external field Δ_b . Consider a phonon Hamiltonian:

$$H_0 = \Omega b^\dagger b + \Delta_b b^\dagger + \Delta_b^* b. \quad (\text{D1})$$

Due to Δ_b , the phonon operator has a nonzero expectation value:

$$\langle b \rangle = \frac{1}{Z} \text{Tr} [b e^{-\beta \Omega (b^\dagger + \Delta_b^*/\Omega)(b + \Delta_b/\Omega) + \beta |\Delta_b|^2/\Omega}]$$

$$= \frac{1}{Z} \text{Tr} [(b + \Delta_b/\Omega - \Delta_b/\Omega)$$

$$\times \exp[-\beta \Omega (b^\dagger + \Delta_b^*/\Omega)(b + \Delta_b/\Omega) + \beta |\Delta_b|^2/\Omega]]$$

$$= \frac{-\Delta_b}{\Omega}, \quad (\text{D2})$$

where $Z = \text{Tr} e^{-\beta H_0}$ is the partition function. Similarly, we can obtain the thermal average of two-point operators:

$$\langle b^\dagger b \rangle = \left\langle \left(b^\dagger + \frac{\Delta_b^*}{\Omega} \right) \left(b + \frac{\Delta_b}{\Omega} \right) - \frac{\Delta_b^* b + \Delta_b b^\dagger}{\Omega} - \frac{|\Delta_b|^2}{\Omega^2} \right\rangle$$

$$= n_b(\Omega) + \frac{|\Delta_b|^2}{\Omega^2} \quad (\text{D3})$$

and

$$\langle b^\dagger b^\dagger \rangle = \left\langle \left(b^\dagger + \frac{\Delta_b^*}{\Omega} \right) \left(b^\dagger + \frac{\Delta_b^*}{\Omega} \right) - \frac{2\Delta_b^* b^\dagger}{\Omega} - \frac{\Delta_b^{*2}}{\Omega^2} \right\rangle = \frac{\Delta_b^{*2}}{\Omega^2}$$

$$\langle bb \rangle = \frac{\Delta_b^2}{\Omega^2}. \quad (\text{D4})$$

Based on these relations, we can compute the phonon Green's function:

$$D(\tau) \equiv -\langle T_\tau A(\tau) A(0) \rangle, \quad (\text{D5})$$

where

$$A(\tau) = e^{\tau \Omega (b^\dagger + \frac{\Delta_b^*}{\Omega})(b + \frac{\Delta_b}{\Omega})} (b + b^\dagger) e^{-\tau \Omega (b^\dagger + \frac{\Delta_b^*}{\Omega})(b + \frac{\Delta_b}{\Omega})}$$

$$= \left(b^\dagger + \frac{\Delta_b^*}{\Omega} \right) e^{\tau \Omega} + \left(b + \frac{\Delta_b}{\Omega} \right) e^{-\tau \Omega} - \frac{\Delta_b^* + \Delta_b}{\Omega}. \quad (\text{D6})$$

Thus for $\tau > 0$, we have

$$\begin{aligned}
D(\tau) &= -\left\langle \left[\left(b^\dagger + \frac{\Delta_b^*}{\Omega} \right) e^{\tau\Omega} + \left(b + \frac{\Delta_b}{\Omega} \right) e^{-\tau\Omega} - \frac{\Delta_b^* + \Delta_b}{\Omega} \right] (b^\dagger + b) \right\rangle \\
&= -\left\langle \left(b^\dagger + \frac{\Delta_b^*}{\Omega} \right) e^{\tau\Omega} b + \left(b + \frac{\Delta_b}{\Omega} \right) e^{-\tau\Omega} b^\dagger \right\rangle + \frac{(\Delta_b^* + \Delta_b) \langle b^\dagger + b \rangle}{\Omega} \\
&= -\{n_B(\Omega)e^{\tau\Omega} + [1 + n_B(\Omega)]e^{-\tau\Omega}\} - \frac{(\Delta_b^* + \Delta_b)^2}{\Omega^2}, \tag{D7}
\end{aligned}$$

such that we can obtain the Green's function in terms of Matsubara frequency by the Fourier transformation:

$$\begin{aligned}
\tilde{D}(i\omega_n) &= \int_0^\beta d\tau e^{i\omega_n\tau} D(\tau) \\
&= \left(\frac{1}{i\omega_n - \Omega} - \frac{1}{i\omega_n + \Omega} \right) - \delta_{\omega_n,0} \frac{\beta(\Delta_b^* + \Delta_b)^2}{\Omega^2}. \tag{D8}
\end{aligned}$$

APPENDIX E: DERIVATION OF EQ. (56)

In this section, we present the steps to obtain Eq. (56). We first apply the perturbation theory to second order such that for a state with eigenenergy ξ^{v_1} we can write the eigenvector as follows:

$$\begin{aligned}
t_{v_2\mathbf{k}}^{v_1} &= \delta_{v_1v_2} \left(1 - \frac{1}{2} \sum_{c_1} \frac{|\Delta_{\mathbf{k}}^{c_1v_1}|^2}{|\xi_{\mathbf{k}}^{v_1} - \xi_{\mathbf{k}+\mathbf{M}}^{c_1}|^2} \right) \\
&+ \sum_{c_1} \frac{(1 - \delta_{v_1v_2}) \Delta_{\mathbf{k}}^{c_1v_2*} \Delta_{\mathbf{k}}^{c_1v_1}}{(\xi_{\mathbf{k}}^{v_1} - \xi_{\mathbf{k}}^{v_2})(\xi_{\mathbf{k}}^{v_1} - \xi_{\mathbf{k}+\mathbf{M}}^{c_1})} \tag{E1}
\end{aligned}$$

and

$$t_{c_1\mathbf{k}}^{v_1} = \frac{\Delta_{\mathbf{k}}^{c_1v_1}}{\xi_{\mathbf{k}}^{v_1} - \xi_{\mathbf{k}+\mathbf{M}}^{c_1}}, \tag{E2}$$

where we use the band index for the new state as mentioned in the main text. Therefore, the absolute square becomes the following:

$$\begin{aligned}
|t_{v_2\mathbf{k}}^{v_1}|^2 &= \delta_{v_1v_2} \left(1 - \sum_{c_1} \frac{|\Delta_{\mathbf{k}}^{c_1v_1}|^2}{|\xi_{\mathbf{k}}^{v_1} - \xi_{\mathbf{k}+\mathbf{M}}^{c_1}|^2} \right) \\
|t_{c_1\mathbf{k}}^{v_1}|^2 &= \frac{|\Delta_{\mathbf{k}}^{c_1v_1}|^2}{|\xi_{\mathbf{k}}^{v_1} - \xi_{\mathbf{k}+\mathbf{M}}^{c_1}|^2}, \tag{E3}
\end{aligned}$$

which simplifies the Eq. (53) to the second order of $\Delta_{\mathbf{k}}$ as

$$\begin{aligned}
U^{(e)} &\approx \sum_{\mathbf{k}\mathbf{q}\mathbf{v}} \left[\sum_{v_1v_2} I(\xi_{\mathbf{k}+\mathbf{q}}^{v_2}, \xi_{\mathbf{k}}^{v_1}, \Omega_{\mathbf{q}\mathbf{v}}) |t_{v_1\mathbf{k}}^{v_1}|^2 |g_{v_2v_1v}(\mathbf{k}, \mathbf{q})|^2 \right. \\
&+ \left. \sum_{c_1c_2} I(\xi_{\mathbf{k}+\mathbf{q}+\mathbf{M}}^{c_2}, \xi_{\mathbf{k}+\mathbf{M}}^{c_1}, \Omega_{\mathbf{q}\mathbf{v}}) |t_{c_1\mathbf{k}}^{c_1}|^2 |g_{c_2c_1v}(\mathbf{k} + \mathbf{M}, \mathbf{q})|^2 \right], \tag{E4}
\end{aligned}$$

where we keep the $\Delta_{\mathbf{k}}^{cv}$ dependence on the states with momentum (\mathbf{k}) and reduce the $t_{v_2\mathbf{k}+\mathbf{q}}^{v_1} (t_{c_2\mathbf{k}+\mathbf{q}}^{c_1})$ to the Kronecker delta

function. Now we can compute the derivative respective to $|\Delta_{\mathbf{k}}^{cv}|$:

$$\begin{aligned}
\frac{\partial U^{(e)}}{\partial |\Delta_{\mathbf{k}}^{cv}|} &= \frac{-2|\Delta_{\mathbf{k}}^{cv}|}{(\xi_{\mathbf{k}+\mathbf{M}}^c - \xi_{\mathbf{k}}^v)^2} \\
&\times \sum_{\mathbf{q}\mathbf{v}} \left[\sum_{v_2} I(\xi_{\mathbf{k}+\mathbf{q}}^{v_2}, \xi_{\mathbf{k}}^v, \Omega_{\mathbf{q}\mathbf{v}}) |g_{v_2v_1v}(\mathbf{k}, \mathbf{q})|^2 \right. \\
&+ \left. \sum_{c_2} I(\xi_{\mathbf{k}+\mathbf{q}+\mathbf{M}}^{c_2}, \xi_{\mathbf{k}+\mathbf{M}}^c, \Omega_{\mathbf{q}\mathbf{v}}) |g_{c_2c_1v}(\mathbf{k} + \mathbf{M}, \mathbf{q})|^2 \right]. \tag{E5}
\end{aligned}$$

To change the variable from Δ^{cv} to χ^{cv} , we apply the small Δ^{cv} expansion to the definition Eq. (34b) such that in the lowest order they follow the relation:

$$\chi_{\mathbf{k}}^{cv} = \frac{\Delta_{\mathbf{k}}^{cv*}}{\xi_{\mathbf{k}+\mathbf{M}}^c - \xi_{\mathbf{k}}^v} (f_{\mathbf{k}+\mathbf{M},c} - f_{\mathbf{k},v}). \tag{E6}$$

Therefore, we can use the chain rule to derive the derivative with respect to χ^{cv} and get Eq. (56):

$$\begin{aligned}
\frac{\partial U^{(e)}}{\partial \chi_{\mathbf{k}}^{cv}} &= \frac{\Delta_{\mathbf{k}}^{cv}}{(\xi_{\mathbf{k}+\mathbf{M}}^c - \xi_{\mathbf{k}}^v)(f_{\mathbf{k}+\mathbf{M},c} - f_{\mathbf{k},v})} \\
&\times \sum_{\mathbf{q}\mathbf{v}} \left[\sum_{v_2} I(\xi_{\mathbf{k}+\mathbf{q}}^{v_2}, \xi_{\mathbf{k}}^v, \Omega_{\mathbf{q}\mathbf{v}}) |g_{v_2v_1v}(\mathbf{k}, \mathbf{q})|^2 \right. \\
&+ \left. \sum_{c_2} I(\xi_{\mathbf{k}+\mathbf{M}+\mathbf{q}}^{c_2}, \xi_{\mathbf{k}+\mathbf{M}}^c, \Omega_{\mathbf{q}\mathbf{v}}) |g_{c_2c_1v}(\mathbf{k} + \mathbf{M}, \mathbf{q})|^2 \right]. \tag{E7}
\end{aligned}$$

APPENDIX F: NUMERICAL DETAIL

For the DFT and DFPT calculations, we employ a Γ -centered $36 \times 36 \times 1$ k grid for BZ sampling and a 85 Ry kinetic energy cutoff for electron density in the self-consistent (scf) calculation with spin-orbit coupling (SOC). By keeping the interlayer vacuum $c = 12.5$ Å to mimic single-layer system, we obtained a relaxed lattice constant $a = 3.545$ Å in agreement with experimental observation $a_{\text{exp.}} = 3.538$ Å [127]. For the GW correction, based on an alternative scf calculation, we adopt a $20 \times 20 \times 1$ k grid and 96 real frequency points to sample the dynamical screening. We conduct the self-consistent GW0 calculation with 200 empty bands included and reach convergence in four iterations. For the anharmonic SCP, we construct a $6 \times 6 \times 1$ supercell to compute the interatomic force without SOC and use the least absolute

shrinkage and selection operator method to extract the anharmonic ph-ph coupling constant. Last, the gap equation is

computed with six conduction bands and six valance bands on a $60 \times 60 \times 1$ k grid with SOC.

-
- [1] J. Bardeen, L. N. Cooper, and J. R. Schrieffer, Microscopic theory of superconductivity, *Phys. Rev.* **106**, 162 (1957).
- [2] N. F. Mott, The transition to the metallic state, *Philos. Mag.* **6**, 287 (1961).
- [3] L. V. Keldysh and Y. V. Kopaev, Possible instability of semimetallic state toward coulomb interaction, *Sov. Phys. Solid State* **6**, 2219 (1965).
- [4] D. Jérôme, T. M. Rice, and W. Kohn, Excitonic insulator, *Phys. Rev.* **158**, 462 (1967).
- [5] B. I. Halperin and T. M. Rice, Possible anomalies at a semimetal-semiconductor transition, *Rev. Mod. Phys.* **40**, 755 (1968).
- [6] F. X. Bronold and H. Fehske, Possibility of an excitonic insulator at the semiconductor-semimetal transition, *Phys. Rev. B* **74**, 165107 (2006).
- [7] Y. Tomio, K. Honda, and T. Ogawa, Excitonic BCS-BEC crossover at finite temperature: Effects of repulsion and electron-hole mass difference, *Phys. Rev. B* **73**, 235108 (2006).
- [8] B. Zenker, D. Ihle, F. X. Bronold, and H. Fehske, Electron-hole pair condensation at the semimetal-semiconductor transition: A bcs-pec crossover scenario, *Phys. Rev. B* **85**, 121102(R) (2012).
- [9] V.-N. Phan, K. W. Becker, and H. Fehske, Exciton condensation due to electron-phonon interaction, *Phys. Rev. B* **88**, 205123 (2013).
- [10] M. De Giorgi, M. Ramezani, F. Todisco, A. Halpin, D. Caputo, A. Fieramosca, J. Gomez-Rivas, and D. Sanvitto, Interaction and coherence of a plasmon-exciton polariton condensate, *ACS Photon.* **5**, 3666 (2018).
- [11] Y. Murakami, D. Golez, M. Eckstein, and P. Werner, Photoinduced enhancement of excitonic order, *Phys. Rev. Lett.* **119**, 247601 (2017).
- [12] J. Neuenschwander and P. Wachter, Pressure-driven semiconductor-metal transition in intermediate-valence $\text{TmSe}_{1-x}\text{Te}_x$ and the concept of an excitonic insulator, *Phys. Rev. B* **41**, 12693 (1990).
- [13] B. Bucher, P. Steiner, and P. Wachter, Excitonic insulator phase in $\text{TmSe}_{0.45}\text{Te}_{0.55}$, *Phys. Rev. Lett.* **67**, 2717 (1991).
- [14] J. Eisenstein and A. MacDonald, Bose-Einstein condensation of excitons in bilayer electron systems, *Nature (Lond.)* **432**, 691 (2004).
- [15] J. I. A. Li, T. Taniguchi, K. Watanabe, J. Hone, A. Levchenko, and C. R. Dean, Negative coulomb drag in double bilayer graphene, *Phys. Rev. Lett.* **117**, 046802 (2016).
- [16] L. Du, X. Li, W. Lou, G. Sullivan, K. Chang, J. Kono, and R.-R. Du, Evidence for a topological excitonic insulator in InAs/GaSb bilayers, *Nat. Commun.* **8**, 1971 (2017).
- [17] S. Gupta, A. Kutana, and B. I. Yakobson, Heterobilayers of 2d materials as a platform for excitonic superfluidity, *Nat. Commun.* **11**, 2989 (2020).
- [18] L. Ma, P. X. Nguyen, Z. Wang, Y. Zeng, K. Watanabe, T. Taniguchi, A. H. MacDonald, K. F. Mak, and J. Shan, Strongly correlated excitonic insulator in atomic double layers, *Nature (Lond.)* **598**, 585 (2021).
- [19] K. Okazaki, Y. Ogawa, T. Suzuki, T. Yamamoto, T. Someya, S. Michimae, M. Watanabe, Y. Lu, M. Nohara, H. Takagi *et al.*, Photo-induced semimetallic states realised in electron-hole coupled insulators, *Nat. Commun.* **9**, 4322 (2018).
- [20] Y. Jia, P. Wang, C.-L. Chiu, Z. Song, G. Yu, B. Jäck, S. Lei, S. Klemenz, F. A. Cevallos, M. Onyszczak *et al.*, Evidence for a monolayer excitonic insulator, *Nat. Phys.* **18**, 87 (2022).
- [21] B. Sun, W. Zhao, T. Palomaki, Z. Fei, E. Runburg, P. Malinowski, X. Huang, J. Cenker, Y.-T. Cui, J.-H. Chu *et al.*, Evidence for equilibrium exciton condensation in monolayer WTe_2 , *Nat. Phys.* **18**, 94 (2022).
- [22] K. Seki, Y. Wakasaka, T. Kaneko, T. Toriyama, T. Konishi, T. Sudayama, N. L. Saini, M. Arita, H. Namatame, M. Taniguchi, N. Katayama, M. Nohara, H. Takagi, T. Mizokawa, and Y. Ohta, Excitonic Bose-Einstein condensation in Ta_2NiSe_5 above room temperature, *Phys. Rev. B* **90**, 155116 (2014).
- [23] H. Hedayat, C. J. Sayers, D. Bugini, C. Dallera, D. Wolverson, T. Batten, S. Karbassi, S. Friedemann, G. Cerullo, J. van Wezel, S. R. Clark, E. Carpene, and E. Da Como, Excitonic and lattice contributions to the charge density wave in $1T - \text{TiSe}_2$ revealed by a phonon bottleneck, *Phys. Rev. Res.* **1**, 023029 (2019).
- [24] Y. F. Lu, H. Kono, T. I. Larkin, A. W. Rost, T. Takayama, A. V. Boris, B. Keimer, and H. Takagi, Zero-gap semiconductor to excitonic insulator transition in Ta_2NiSe_5 , *Nat. Commun.* **8**, 14408 (2017).
- [25] K. Sugimoto, S. Nishimoto, T. Kaneko, and Y. Ohta, Strong coupling nature of the excitonic insulator state in Ta_2NiSe_5 , *Phys. Rev. Lett.* **120**, 247602 (2018).
- [26] K. Kim, H. Kim, J. Kim, C. Kwon, J. S. Kim, and B. Kim, Direct observation of excitonic instability in Ta_2NiSe_5 , *Nat. Commun.* **12**, 1969 (2021).
- [27] A. Kogar, M. S. Rak, S. Vig, A. A. Husain, F. Flicker, Y. I. Joe, L. Venema, G. J. MacDougall, T. C. Chiang, E. Fradkin *et al.*, Signatures of exciton condensation in a transition metal dichalcogenide, *Science* **358**, 1314 (2017).
- [28] S. Hellmann, T. Rohwer, M. Kalläne, K. Hanff, C. Sohrt, A. Stange, A. Carr, M. Murnane, H. Kapteyn, L. Kipp *et al.*, Time-domain classification of charge-density-wave insulators, *Nat. Commun.* **3**, 1069 (2012).
- [29] T. E. Kidd, T. Miller, M. Y. Chou, and T.-C. Chiang, Electron-hole coupling and the charge density wave transition in TiSe_2 , *Phys. Rev. Lett.* **88**, 226402 (2002).
- [30] F. Weber, S. Rosenkranz, J.-P. Castellan, R. Osborn, G. Karapetrov, R. Hott, R. Heid, K.-P. Bohnen, and A. Alatas, Electron-phonon coupling and the soft phonon mode in TiSe_2 , *Phys. Rev. Lett.* **107**, 266401 (2011).
- [31] K. Rossnagel, L. Kipp, and M. Skibowski, Charge-density-wave phase transition in $1T - \text{TiSe}_2$: Excitonic insulator versus band-type Jahn-Teller mechanism, *Phys. Rev. B* **65**, 235101 (2002).
- [32] H. Cercellier, C. Monney, F. Clerc, C. Battaglia, L. Despont, M. G. Garnier, H. Beck, P. Aebi, L. Patthey, H. Berger, and L.

- Forró, Evidence for an excitonic insulator phase in 1T-TiSe₂, *Phys. Rev. Lett.* **99**, 146403 (2007).
- [33] M. Holt, P. Zschack, H. Hong, M. Y. Chou, and T.-C. Chiang, X-ray studies of phonon softening in TiSe₂, *Phys. Rev. Lett.* **86**, 3799 (2001).
- [34] H. Hughes, Structural distortion in TiSe₂ and related materials—A possible Jahn-Teller effect?, *J. Phys. C: Solid State Phys.* **10**, L319 (1977).
- [35] N. Suzuki, A. Yamamoto, and K. Motizuki, Microscopic theory of the CDW state of 1T-TiSe₂, *J. Phys. Soc. Jpn.* **54**, 4668 (1985).
- [36] M. H. Whangbo and E. Canadell, Analogies between the concepts of molecular chemistry and solid-state physics concerning structural instabilities. electronic origin of the structural modulations in layered transition metal dichalcogenides, *J. Am. Chem. Soc.* **114**, 9587 (1992).
- [37] J. A. Wilson, A. S. Barker, F. J. Di Salvo, and J. A. Ditzenberger, Infrared properties of the semimetal TiSe₂, *Phys. Rev. B* **18**, 2866 (1978).
- [38] T. Pillo, J. Hayoz, H. Berger, F. Lévy, L. Schlapbach, and P. Aebi, Photoemission of bands above the Fermi level: The excitonic insulator phase transition in 1T-TiSe₂, *Phys. Rev. B* **61**, 16213 (2000).
- [39] C. Monney, H. Cercieller, F. Clerc, C. Battaglia, E. F. Schwier, C. Didiot, M. G. Garnier, H. Beck, P. Aebi, H. Berger, L. Forró, and L. Patthey, Spontaneous exciton condensation in 1T-TiSe₂: BCS-like approach, *Phys. Rev. B* **79**, 045116 (2009).
- [40] J. van Wezel, P. Nahai-Williamson, and S. S. Saxena, Exciton-phonon-driven charge density wave in TiSe₂, *Phys. Rev. B* **81**, 165109 (2010).
- [41] K. Rossnagel, On the origin of charge-density waves in select layered transition-metal dichalcogenides, *J. Phys.: Condens. Matter* **23**, 213001 (2011).
- [42] B. Zenker, H. Fehske, H. Beck, C. Monney, and A. R. Bishop, Chiral charge order in 1T-TiSe₂: Importance of lattice degrees of freedom, *Phys. Rev. B* **88**, 075138 (2013).
- [43] M. Hellgren, J. Baima, R. Bianco, M. Calandra, F. Mauri, and L. Wirtz, Critical role of the exchange interaction for the electronic structure and charge-density-wave formation in TiSe₂, *Phys. Rev. Lett.* **119**, 176401 (2017).
- [44] P. Chen, Y.-H. Chan, X.-Y. Fang, Y. Zhang, M.-Y. Chou, S.-K. Mo, Z. Hussain, A.-V. Fedorov, and T.-C. Chiang, Charge density wave transition in single-layer titanium diselenide, *Nat. Commun.* **6**, 8943 (2015).
- [45] K. Sugawara, Y. Nakata, R. Shimizu, P. Han, T. Hitosugi, T. Sato, and T. Takahashi, Unconventional charge-density-wave transition in monolayer 1T-TiSe₂, *ACS Nano* **10**, 1341 (2016).
- [46] B. Singh, C.-H. Hsu, W.-F. Tsai, V. M. Pereira, and H. Lin, Stable charge density wave phase in a 1T-TiSe₂ monolayer, *Phys. Rev. B* **95**, 245136 (2017).
- [47] D. L. Duong, G. Ryu, A. Hoyer, C. Lin, M. Burghard, and K. Kern, Raman characterization of the charge density wave phase of 1T-TiSe₂: From bulk to atomically thin layers, *ACS Nano* **11**, 1034 (2017).
- [48] X.-Y. Fang, H. Hong, P. Chen, and T.-C. Chiang, X-ray study of the charge-density-wave transition in single-layer TiSe₂, *Phys. Rev. B* **95**, 201409(R) (2017).
- [49] S. Kolekar, M. Bonilla, Y. Ma, H. C. Diaz, and M. Batzill, Layer-and substrate-dependent charge density wave criticality in 1T-TiSe₂, *2D Mater.* **5**, 015006 (2017).
- [50] T. Kaneko, Y. Ohta, and S. Yunoki, Exciton-phonon cooperative mechanism of the triple-*q* charge-density-wave and antiferroelectric electron polarization in TiSe₂, *Phys. Rev. B* **97**, 155131 (2018).
- [51] L. Li, E. O'Farrell, K. Loh, G. Eda, B. Özyilmaz, and A. Castro Neto, Controlling many-body states by the electric-field effect in a two-dimensional material, *Nature (Lond.)* **529**, 185 (2016).
- [52] D. M. Ceperley and B. J. Alder, Ground state of the electron gas by a stochastic method, *Phys. Rev. Lett.* **45**, 566 (1980).
- [53] J. P. Perdew, K. Burke, and M. Ernzerhof, Generalized gradient approximation made simple, *Phys. Rev. Lett.* **77**, 3865 (1996).
- [54] J. Heyd, G. E. Scuseria, and M. Ernzerhof, Hybrid functionals based on a screened coulomb potential, *J. Chem. Phys.* **118**, 8207 (2003).
- [55] M. Hellgren, J. Baima, and A. Acheche, Exciton peierls mechanism and universal many-body gaps in carbon nanotubes, *Phys. Rev. B* **98**, 201103(R) (2018).
- [56] D. Pasquier and O. V. Yazyev, Excitonic effects in two-dimensional TiSe₂ from hybrid density functional theory, *Phys. Rev. B* **98**, 235106 (2018).
- [57] B. Guster, R. Robles, M. Pruneda, E. Canadell, and P. Ordejón, 2 × 2 charge density wave in single-layer TiTe₂, *2D Mater.* **6**, 015027 (2018).
- [58] D. Varsano, M. Palummo, E. Molinari, and M. Rontani, A monolayer transition-metal dichalcogenide as a topological excitonic insulator, *Nat. Nanotechnol.* **15**, 367 (2020).
- [59] T. Kaneko, T. Toriyama, T. Konishi, and Y. Ohta, Electronic structure of Ta₂NiSe₅ as a candidate for excitonic insulators, *J. Phys.: Conf. Ser.* **400**, 032035 (2012).
- [60] S. Conti, A. Perali, F. M. Peeters, and D. Neilson, Multicomponent screening and superfluidity in gapped electron-hole double bilayer graphene with realistic bands, *Phys. Rev. B* **99**, 144517 (2019).
- [61] F. Nilsson and F. Aryasetiawan, Effects of dynamical screening on the BCS-BEC crossover in double bilayer graphene: Density functional theory for exciton bilayers, *Phys. Rev. Mater.* **5**, L050801 (2021).
- [62] D. Varsano, S. Sorella, D. Sangalli, M. Barborini, S. Corni, E. Molinari, and M. Rontani, Carbon nanotubes as excitonic insulators, *Nat. Commun.* **8**, 1461 (2017).
- [63] S. Kurth, M. Marques, M. Luders, and E. K. U. Gross, Local density approximation for superconductors, *Phys. Rev. Lett.* **83**, 2628 (1999).
- [64] M. Luders, M. A. L. Marques, N. N. Lathiotakis, A. Floris, G. Profeta, L. Fast, A. Continenza, S. Massidda, and E. K. U. Gross, Ab initio theory of superconductivity. I. Density functional formalism and approximate functionals, *Phys. Rev. B* **72**, 024545 (2005).
- [65] T. Tadano and S. Tsuneyuki, First-principles lattice dynamics method for strongly anharmonic crystals, *J. Phys. Soc. Jpn.* **87**, 041015 (2018).
- [66] T. Kreibich and E. K. U. Gross, Multicomponent density-functional theory for electrons and nuclei, *Phys. Rev. Lett.* **86**, 2984 (2001).

- [67] U. Von Barth and L. Hedin, A local exchange-correlation potential for the spin polarized case. I, *J. Phys. C: Solid State Phys.* **5**, 1629 (1972).
- [68] L. N. Oliveira, E. K. U. Gross, and W. Kohn, Density-functional theory for superconductors, *Phys. Rev. Lett.* **60**, 2430 (1988).
- [69] W. Kohn and L. J. Sham, Self-consistent equations including exchange and correlation effects, *Phys. Rev.* **140**, A1133 (1965).
- [70] P. Hohenberg and W. Kohn, Inhomogeneous electron gas, *Phys. Rev.* **136**, B864 (1964).
- [71] The effect of NL charge density at zero temperature limit is first discussed in Sec. II B of Ref. [69], where the authors used the Hartree-Fock method to obtain the NL part of the exchange-correlation potential.
- [72] Equation (6) extends the thermodynamic potential derived with local density in Sec. III of Ref. [69]. A similar extension for superconductivity can be found in Eq. (10) of Ref. [64] and Chapter 16 in Ref. [85].
- [73] Using the Hartree-Fock approach to compute the Δ_{xc} , Eq. (13) can be converted to Eq. (2.22) in Ref. [69].
- [74] From here and following, we use ψ to denote the eigen function of KS equation with only local potential and use ϕ for the eigen function of KS equation with nonlocal potential.
- [75] A. Görling and M. Levy, Exact Kohn-Sham scheme based on perturbation theory, *Phys. Rev. A* **50**, 196 (1994).
- [76] J. Goldstone, Derivation of the brueckner many-body theory, *Proc. R. Soc. A: Math. Phys. Eng. Sci.* **239**, 267 (1957).
- [77] G. D. Mahan, *Many-particle Physics* (Springer Science & Business Media, New York, 2013).
- [78] R. D. Mattuck, *A Guide to Feynman Diagrams in the Many-body Problem* (Courier Corporation, North Chelmsford, MA, 1992).
- [79] For a comprehensive introduction of linked-cluster theorem, we refer the readers to sect. 3.6 of Ref. [77] and chapter 15 of Ref. [78].
- [80] M. S. Hybertsen and S. G. Louie, Electron correlation in semiconductors and insulators: Band gaps and quasiparticle energies, *Phys. Rev. B* **34**, 5390 (1986).
- [81] S. Baroni, S. de Gironcoli, A. Dal Corso, and P. Giannozzi, Phonons and related crystal properties from density-functional perturbation theory, *Rev. Mod. Phys.* **73**, 515 (2001).
- [82] M. Bernardi, First-principles dynamics of electrons and phonons, *Eur. Phys. J. B* **89**, 239 (2016).
- [83] M. T. Yin and M. L. Cohen, Microscopic theory of the phase transformation and lattice dynamics of Si, *Phys. Rev. Lett.* **45**, 1004 (1980).
- [84] F. Giustino, Electron-phonon interactions from first principles, *Rev. Mod. Phys.* **89**, 015003 (2017).
- [85] E. Pavarini, E. Koch, R. Martin, and R. Scalettar (eds.), *The Physics of Correlated Insulators, Metals, and Superconductors*, Vol. 7 (Forschungszentrum Jülich, 2017).
- [86] E. Pavarini and E. Koch (eds.), *Topology, Entanglement, and Strong Correlations*, Vol. 10 (Forschungszentrums Jülich, 2020).
- [87] In Eqs. (26a) and (26b), we adopt different notation from conventional usage. Equation (26a) corresponds to the Eq. (137) and Eq. (26a) corresponds to the Eq. (145) in Ref. [84]. The definition of the e -ph coupling can be found in Eqs. (34) and (38) in Ref. [84], or a equivalent but clear form in Eq. (10) in Ref. [82]. A comprehensive introduction can be found in chapter 15 of Ref. [85] and chapter 14 of Ref. [86].
- [88] J. Berges, E. G. C. P. van Loon, A. Schobert, M. Rösner, and T. O. Wehling, Ab initio phonon self-energies and fluctuation diagnostics of phonon anomalies: Lattice instabilities from dirac pseudospin physics in transition metal dichalcogenides, *Phys. Rev. B* **101**, 155107 (2020).
- [89] M. Bernardi, D. Vigil-Fowler, J. Lischner, J. B. Neaton, and S. G. Louie, Ab initio study of hot carriers in the first picosecond after sunlight absorption in silicon, *Phys. Rev. Lett.* **112**, 257402 (2014).
- [90] N.-E. Lee, J.-J. Zhou, L. A. Agapito, and M. Bernardi, Charge transport in organic molecular semiconductors from first principles: The bandlike hole mobility in a naphthalene crystal, *Phys. Rev. B* **97**, 115203 (2018).
- [91] J.-J. Zhou and M. Bernardi, Predicting charge transport in the presence of polarons: The beyond-quasiparticle regime in SrTiO₃, *Phys. Rev. Res.* **1**, 033138 (2019).
- [92] T. Tadano, Y. Gohda, and S. Tsuneyuki, Anharmonic force constants extracted from first-principles molecular dynamics: applications to heat transfer simulations, *J. Phys.: Condens. Matter* **26**, 225402 (2014).
- [93] T. Tadano and S. Tsuneyuki, Self-consistent phonon calculations of lattice dynamical properties in cubic SrTiO₃ with first-principles anharmonic force constants, *Phys. Rev. B* **92**, 054301 (2015).
- [94] W. Sano, T. Koretsune, T. Tadano, R. Akashi, and R. Arita, Effect of van Hove singularities on high- T_c superconductivity in H₃S, *Phys. Rev. B* **93**, 094525 (2016).
- [95] J.-J. Zhou, O. Hellman, and M. Bernardi, Electron-phonon scattering in the presence of soft modes and electron mobility in SrTiO₃ perovskite from first principles, *Phys. Rev. Lett.* **121**, 226603 (2018).
- [96] T. Wang, J. A. Flores-Livas, T. Nomoto, Y. Ma, T. Koretsune, and R. Arita, Optimal alloying in hydrides: Reaching room-temperature superconductivity in LaH₁₀, *Phys. Rev. B* **105**, 174516 (2022).
- [97] R. Masuki, T. Nomoto, R. Arita, and T. Tadano, Ab initio structural optimization at finite temperatures based on anharmonic phonon theory: Application to the structural phase transitions of BaTiO₃, *Phys. Rev. B* **106**, 224104 (2022).
- [98] I. Errea, M. Calandra, and F. Mauri, Anharmonic free energies and phonon dispersions from the stochastic self-consistent harmonic approximation: Application to platinum and palladium hydrides, *Phys. Rev. B* **89**, 064302 (2014).
- [99] Compared to the Eq. (30) in the Chapter 14 of Ref. [86], here we follow the Ref. [65] and write the expansion in momentum space.
- [100] For here and Eq. (52), we use the matrix form to write the normal/anomalous Green's function. They are physically equivalent to Eq. (3.6) and Eq. (3.8) in Ref. [4].
- [101] A more comprehensive treatment of Coulomb screening should incorporate the consideration of dynamical interband transitions and intraband screening when the energy gap closes in a metallic phase. However, in practice, the former is often approximated by static screening in GW-BSE methods, while the latter is notably weak in the temperature regime below T_c , due to the insulating behavior of the ordered phase. For more

- detail on RPA and screened Coulomb interaction, we suggest chapter 11 of Ref. [125].
- [102] J. S. Zhou, L. Monacelli, R. Bianco, I. Errea, F. Mauri, and M. Calandra, Anharmonicity and doping melt the charge density wave in single-layer TiSe_2 , *Nano Lett.* **20**, 4809 (2020).
- [103] P. Giannozzi, S. Baroni, N. Bonini, M. Calandra, R. Car, C. Cavazzoni, D. Ceresoli, G. L. Chiarotti, M. Cococcioni, I. Dabo *et al.*, Quantum espresso: A modular and open-source software project for quantum simulations of materials, *J. Phys.: Condens. Matter* **21**, 395502 (2009).
- [104] N. Troullier and J. L. Martins, Efficient pseudopotentials for plane-wave calculations, *Phys. Rev. B* **43**, 1993 (1991).
- [105] M. J. van Setten, M. Giantomassi, E. Bousquet, M. J. Verstraete, D. R. Hamann, X. Gonze, and G.-M. Rignanese, The pseudodojo: Training and grading a 85 element optimized norm-conserving pseudopotential table, *Comput. Phys. Commun.* **226**, 39 (2018).
- [106] G. Kresse and J. Furthmüller, Efficient iterative schemes for ab initio total-energy calculations using a plane-wave basis set, *Phys. Rev. B* **54**, 11169 (1996).
- [107] A. A. Mostofi, J. R. Yates, G. Pizzi, Y.-S. Lee, I. Souza, D. Vanderbilt, and N. Marzari, An updated version of wannier90: A tool for obtaining maximally-localised wannier functions, *Comput. Phys. Commun.* **185**, 2309 (2014).
- [108] D. L. Duong, M. Burghard, and J. C. Schön, Ab initio computation of the transition temperature of the charge density wave transition in TiSe_2 , *Phys. Rev. B* **92**, 245131 (2015).
- [109] A. Subedi, Trigonal-to-monoclinic structural transition in TiSe_2 due to a combined condensation of $q = (\frac{1}{2}, 0, 0)$ and $(\frac{1}{2}, 0, \frac{1}{2})$ phonon instabilities, *Phys. Rev. Mater.* **6**, 014602 (2022).
- [110] J.-J. Zhou, J. Park, I.-T. Lu, I. Maliyov, X. Tong, and M. Bernardi, Perturbo: A software package for ab initio electron-phonon interactions, charge transport and ultrafast dynamics, *Comput. Phys. Commun.* **264**, 107970 (2021).
- [111] This triple- q extension is consistent with the formalism presented in Ref. [39]. The left-hand side of Eq. (65) can generate the mean-field Green's function of Eq. (6) in Ref. [39].
- [112] R. Micnas, J. Ranninger, and S. Robaszkiewicz, Superconductivity in narrow-band systems with local nonretarded attractive interactions, *Rev. Mod. Phys.* **62**, 113 (1990).
- [113] N. Lopes, M. A. Continentino, and D. G. Barci, Excitonic insulators and Gross-Neveu models, *Phys. Rev. B* **105**, 165125 (2022).
- [114] D. Sangalli, A. Ferretti, H. Miranda, C. Attaccalite, I. Marri, E. Cannuccia, P. Melo, M. Marsili, F. Paleari, A. Marrazzo *et al.*, Many-body perturbation theory calculations using the yambo code, *J. Phys.: Condens. Matter* **31**, 325902 (2019).
- [115] N. D. Mermin and H. Wagner, Absence of ferromagnetism or antiferromagnetism in one- or two-dimensional isotropic Heisenberg models, *Phys. Rev. Lett.* **17**, 1133 (1966).
- [116] J. M. Kosterlitz and D. J. Thouless, Ordering, metastability and phase transitions in two-dimensional systems, *J. Phys. C: Solid State Phys.* **6**, 1181 (1973).
- [117] W. Kohn and D. Sherrington, Two kinds of bosons and bose condensates, *Rev. Mod. Phys.* **42**, 1 (1970).
- [118] R. R. Guseinov and L. V. Keldysh, Nature of the phase transition under the conditions of an "excitonic" instability in the electronic spectrum of a crystal, *Sov. Phys. JETP* **36** (1973).
- [119] P. Littlewood, P. Eastham, J. Keeling, F. Marchetti, B. Simons, and M. Szymanska, Models of coherent exciton condensation, *J. Phys.: Condens. Matter* **16**, S3597 (2004).
- [120] It is worth noting that a particular exception arises in the case of exciton condensation within the bilayer heterostructure [14]. In this scenario, the electron and hole are spatially separated, and their respective particle numbers are conserved. The corresponding continuous phase rotational symmetry is broken during the condensation of exciton so that the phase transition is restrained by Mermin-Wagner theorem.
- [121] E. Morosan, H. W. Zandbergen, B. Dennis, J. Bos, Y. Onose, T. Klimczuk, A. Ramirez, N. Ong, and R. J. Cava, Superconductivity in Cu_xTiSe_2 , *Nat. Phys.* **2**, 544 (2006).
- [122] P. Goli, J. Khan, D. Wickramaratne, R. K. Lake, and A. A. Balandin, Charge density waves in exfoliated films of van der Waals materials: Evolution of Raman spectrum in TiSe_2 , *Nano Lett.* **12**, 5941 (2012).
- [123] R. W. Godby and R. J. Needs, Metal-insulator transition in Kohn-Sham theory and quasiparticle theory, *Phys. Rev. Lett.* **62**, 1169 (1989).
- [124] P. Larson, M. Dvorak, and Z. Wu, Role of the plasmon-pole model in the *GW* approximation, *Phys. Rev. B* **88**, 125205 (2013).
- [125] R. M. Martin, L. Reining, and D. M. Ceperley, *Interacting Electrons* (Cambridge University Press, Cambridge, UK, 2016).
- [126] For more pedagogic derivation for *GW* using Green's function approach. We refer the reader to the chapter 11 of Ref. [125].
- [127] J.-P. Peng, J.-Q. Guan, H.-M. Zhang, C.-L. Song, L. Wang, K. He, Q.-K. Xue, and X.-C. Ma, Molecular beam epitaxy growth and scanning tunneling microscopy study of TiSe_2 ultrathin films, *Phys. Rev. B* **91**, 121113(R) (2015).